

# Intelligent characterisation of space objects with hyperspectral imaging

Massimiliano Vasile<sup>a,\*</sup>, Lewis Walker<sup>a</sup>, R. David Dunphy<sup>b</sup>, Jaime Zabalza<sup>b</sup>, Paul Murray<sup>b</sup>, Stephen Marshall<sup>b</sup>, Vasili Savitski<sup>c</sup>

<sup>a</sup> Department of Mechanical and Aerospace Engineering, University of Strathclyde, 75 Montrose Street, Glasgow, G11XJ, UK

<sup>b</sup> Department of Electrical and Electronics Engineering, University of Strathclyde, Royal College Building 204 George Street, Glasgow, G11XW, UK

<sup>c</sup> Fraunhofer Centre for Applied Photonics, 99 George Street, Glasgow, G11RD, UK

## ARTICLE INFO

### Keywords:

Hyperspectral imaging  
Machine learning  
Space debris  
Attitude motion

## ABSTRACT

This paper presents some initial results on the use of hyperspectral imaging technology and machine learning to characterise the surface composition of space objects and reconstruct their attitude motion. The paper provides a preliminary demonstration that hyperspectral and multispectral analysis of the light absorbed, emitted and reflected by space objects can be used to identify, with some degree of accuracy, the materials composing their surface. The paper introduces a high-fidelity simulation model, developed to test this concept, and a validation of the model against experimental tests in a laboratory environment. The paper shows how to unmix the spectra to provide an estimation of the materials composing the surface facing the sensor. A machine learning approach is then proposed to reconstruct the attitude motion from the time series of spectra.

## 1. Introduction

The use of spectroscopy, spectral analysis and colour photometry to characterise the composition of space objects have been proposed since the late nineties [1–7]. Although in these references the authors considered the use of spectroscopy for the characterisation of the material composition of space objects, the work was mainly observational: spectra were observed for known objects and were associated to material types. A first classification approach based on colour indexes and on the characteristics of the spectra has also been proposed, see for example [4,6]. Likewise, the use of colour photometry in [5] was proposed to differentiate between different objects but not used to identify materials on different surfaces or reconstruct the attitude motion. At the same time, the use of hyperspectral technology and spectrometry have found important applications in astronomy, to classify and characterise asteroids [8] for example. In parallel, a body of work has focused on the use of light curve analysis to reconstruct the attitude motion or the shape of space objects [9–14]. More recently, Machine Learning (ML) was introduced to classify objects starting from their light curves [15,16]. Hyperspectral imaging for close-proximity navigation was studied in [17] and some literature exists on the use of hyperspectral imaging for the identification and classification of targets on ground [18]. Furthermore, a large body of work exists on the use of hyperspectral imaging for various applications in Earth Observation.

This paper will present some preliminary results on the use of hyperspectral imaging techniques to infer the surface composition of space

objects and estimate their attitude motion. As previously done with spectroscopy, the core idea is to analyse the spectral composition of the light reflected and emitted by each surface of a space object to identify the materials composing that surface. By tracking the variation of the intensity at different wavelengths over time, one can then identify the attitude motion. The end goal is to associate a material distribution and a pointing direction to a given surface at any one time.

The work in this paper differs from the existing literature on spectroscopy of space objects in two ways: (i) it proposes a signal processing technique used in hyperspectral imaging to unmix the spectral composition of the received light and estimate the relative abundance of materials on the surface facing the sensor and (ii) it demonstrates the use of machine learning to estimate the attitude motion by associating time series of spectral responses to the corresponding quaternion time history.

The paper will first present a high-fidelity simulation model of the variation of intensity per wavelength. We will consider both the case in which the sensor is in space and the one in which the sensor is on Earth. For the latter, we will include the attenuation introduced by the atmosphere at different elevation angles. The high-fidelity model was essential to experiment with the unmixing of the spectra and the attitude reconstruction from spectra time series. Alongside the high-fidelity model, some laboratory experiments were used to calibrate the model and assess the feasibility of detecting different materials on different surfaces. After the description of the laboratory experiments,

\* Corresponding author.

E-mail address: [massimiliano.vasile@strath.ac.uk](mailto:massimiliano.vasile@strath.ac.uk) (M. Vasile).

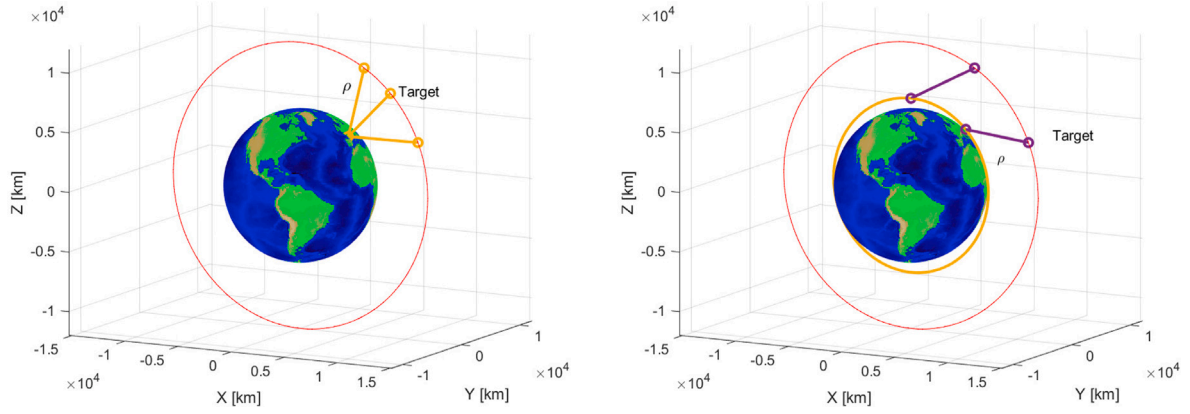


Fig. 1. Earth reference frame and position vector. For each of the two cases, a few observer-to-target vectors  $\rho$  are represented.

the paper will present a methodology to unmix the spectra and relate the unmixed spectra to the attitude motion of an object. We will focus on an equivalent cube and test the idea on a nanosat in orbit and observed either from ground or from a sensor in space. The paper will then show how one can train a machine learning algorithm to reconstruct the attitude from the time series of the spectra.

## 2. Simulation framework

In order to develop the signal processing methodology that is required to characterise objects from their light curve decomposition, we developed a high fidelity simulator of the light emitted and reflected by the surface of objects in space. The simulator implements a six-degrees-of-freedom dynamic model used to propagate both orbital and rotational motion, as well as a model of the position of the observer. The observer can either be a telescope on the ground or a satellite in orbit. This allows all auxiliary quantities required to be calculated directly from the state vector at time  $t$  corresponding to individual exposures of the hyperspectral imaging system. For observations acquired from ground, we included the attenuation effect of the atmosphere. No weathering effects on the materials in orbit have yet been included [2]. Although the space environment has been shown to affect the reflectance spectra of satellites over extended periods of time, where they exhibit a fairly significant ‘redenning’ of the spectra [19], the process is not yet understood well enough to incorporate aging into the simulation model. However, it is trivial to update the reflectance spectra in the model’s library, for example to use spectra corresponding to a particular exposure duration, once these effects are better understood and can be accurately modelled.

### 2.1. Observer and target equations of motion

The position of the observed object, the target, is defined in an Earth Centred Inertial (ECI) reference frame at epoch by the vector  $\mathbf{r}_t = [x_t, y_t, z_t]^T$ . The observer is defined in the same reference frame by the vector  $\mathbf{r}_o = [x_o, y_o, z_o]^T$ . The observer to target vector is simply  $\rho = \mathbf{r}_t - \mathbf{r}_o$ . For observations acquired from ground, the position of the observer is defined by its latitude and longitude, assuming that the Earth rotates around the  $z$ -axis with constant angular velocity  $\omega_E$ . Thus, the components of the position of the observer are defined as  $\mathbf{r}_o = [R_E \cos l \cos(\omega_E t), R_E \cos l \sin(\omega_E t), R_E \sin l]^T$ , where  $l$  is the latitude and  $R_E$  is the mean Earth radius. The target is assumed to move of pure Keplerian motion, thus the second time derivative of its position vector is given by:

$$\ddot{\mathbf{r}}_t = -\frac{\mu_E \mathbf{r}_t}{r_t^3} \quad (1)$$

with  $r_t$  the norm of  $\mathbf{r}_t$  and  $\mu_E$  the gravity constant of the Earth. For observations acquired from space, the observer is assumed to move of

purely Keplerian motion and subject to the same governing equation in Eq. (1). No attitude of the in-orbit observer was simulated. The two types of simulation with observer on the ground or in space are depicted in Fig. 1.

The target is assumed to be a rigid body with free attitude dynamics defined in a principal axis body frame by:

$$\mathbf{I}\dot{\boldsymbol{\omega}} = -\boldsymbol{\omega} \wedge \mathbf{I}\boldsymbol{\omega} \quad (2)$$

with the kinematics expressed in quaternions:

$$\dot{\mathbf{q}} = \frac{1}{2} \boldsymbol{\Omega} \mathbf{q} \quad (3)$$

where  $\boldsymbol{\Omega}$  is the skew symmetric matrix:

$$\boldsymbol{\Omega} = \begin{bmatrix} 0 & -\omega_1 & -\omega_2 & -\omega_3 \\ \omega_1 & 0 & \omega_3 & -\omega_2 \\ \omega_2 & -\omega_3 & 0 & \omega_1 \\ \omega_3 & \omega_2 & -\omega_1 & 0 \end{bmatrix} \quad (4)$$

Eqs. (1), (2) and (3) are propagated using discrete time steps corresponding to each sample time of the sensor using Matlab’s ode45 solver. Quaternions are then converted into Euler angles to identify which face is illuminated and the projection on the target–observer direction.

### 2.2. Light emission and reflection model

Objects are represented by a triangulated point cloud in .obj format, with information about the material corresponding to each face stored in its RGB colour value. This allows the correct material properties and reflectance spectra to be paired with each element in the model at a later stage.

Light reflection is modelled as entirely diffuse, following Lambert’s cosine law: the light reflected by a surface element of area  $dA$  falls with the cosine of the angle  $\theta_0$  between the local surface element normal and the direction of the observer (see Fig. 2). Explicitly, for an aperture which subtends a solid angle  $d\theta$  from the viewpoint of a given surface element, the collected light power is calculated according to:

$$P(\theta) = P_0 \cos \theta_0 dA d\theta \quad (5)$$

where the power per unit solid angle per unit surface area in the normal direction can be calculated by integrating over a hemisphere:

$$P_0 = \frac{RP_{inc} \cos \theta_i}{\pi} \quad (6)$$

where  $P_{inc}$  is the intensity of incident light,  $\theta_i$  is the angle between the direction of incident light  $\hat{\mathbf{S}}$  and the local normal  $\mathbf{n}$ , and  $R$  is the reflectivity of the material comprising the element. By defining  $P_{inc}(\lambda)$  and  $R(\lambda)$  as a function of the wavelength  $\lambda$ , Eq. (5) returns the spectrum received from each surface element.

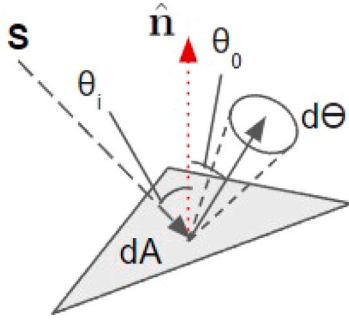


Fig. 2. Illustration of the Lambertian reflectance model. The amount of light reflected into solid angle  $d\Theta$  is dependent only on the angle  $\theta_o$  from the local surface normal, and is axisymmetric about  $\hat{n}$ .

Making this substitution, and integrating across some finite wavelength band defined by the sensor, the total collected power from some element  $e$  is:

$$dP_R^{(e)}|_{\lambda_0+d\lambda} = \frac{\cos \theta_i^{(e)} \cos \theta_o^{(e)} d\Theta dA^{(e)}}{\pi} \int_{\lambda_0}^{\lambda_0+d\lambda} R_{m_e}(\lambda) P_{inc}(\lambda) d\lambda \quad (7)$$

where the subscript  $m_e$  denotes the material comprising element  $e$  and implies that different materials will have different shaped curves  $R_{m_e}(\lambda)$ . The total collected power in the band due to light reflection  $P_R|_{\lambda_0+d\lambda}$  is then simply a sum over elements  $e$  in the triangulation, multiplied by a term  $s_s^{(e)} s_o^{(e)}$  which reduces an element's contribution according to its visibility from the location of the illumination source and the observer:

$$P_R|_{\lambda_0+d\lambda} = \sum_e s_s^{(e)} s_o^{(e)} dP_R^{(e)}|_{\lambda_0+d\lambda} \quad (8)$$

The terms  $s_s^{(e)}$  and  $s_o^{(e)}$  are defined by looking at each vertex in the 3D model, and determining if it has a clear line of sight to the illumination source and the observer respectively, unobstructed by the object's own geometry. Since each element has three vertices, the contribution from element  $e$  is reduced by  $\frac{1}{3}$  times the number of occluded vertices. Thus, both  $s_s^{(e)}$  and  $s_o^{(e)}$  take values in the set  $[0, \frac{1}{3}, \frac{2}{3}, 1]$ . For example, if one vertex is occluded from the viewpoint of the observer,  $s_o^{(e)} = \frac{2}{3}$ , as illustrated in Fig. 3. The total reduction to the power contribution of element  $e$  is then their product  $s_s^{(e)} s_o^{(e)}$ . This approach was chosen over a triangle-ray intersection algorithm with respect to element centroids due to computation speed. Additionally, although imperfect (shadowing of one vertex does not always reduce the effective area by exactly  $\frac{1}{3}$ ), this approach offers a higher degree of detail than binary visibility based on the centroid, for equivalent polygon size. Point visibility with respect to the two viewpoints is determined using Katz' hidden point removal algorithm [20]. As a precaution for elements residing on sharp edges, back-face culling was used to set  $s_s^{(e)}$  and/or  $s_o^{(e)}$  to zero if  $\theta_i$  and/or  $\theta_o$  are greater than 90 degrees, respectively.

A similar expression exists for the emitted light. In this case, the integral term in Eq. (8) is replaced with an integral of the black body spectrum over the band, multiplied by the emissivity  $\epsilon_m$  of material  $m$ . Since element visibility in the context of emitted light does not depend on the source direction, the factor  $s_s^{(e)}$  is also removed. Making these modifications to Eqs. (7) and (8), we have the equations for the emission component:

$$dP_E|_{\lambda_0+d\lambda} = \sum_e \frac{\cos \theta_o^{(e)} d\Theta dA^{(e)} \epsilon_m^{(e)}}{\pi} \int_{\lambda_0}^{\lambda_0+d\lambda} B_\lambda(\lambda, T) d\lambda \quad (9)$$

and

$$P_E|_{\lambda_0+d\lambda} = \sum_e s_o^{(e)} dP_E^{(e)}|_{\lambda_0+d\lambda} \quad (10)$$

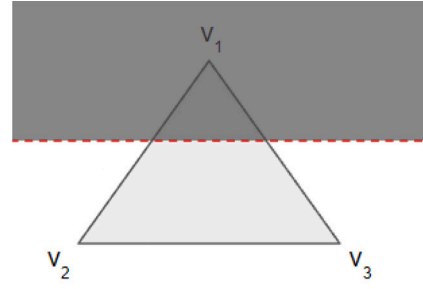


Fig. 3. Illustration of vertex-based partial element visibility model. If only vertex  $v_1$  is in shadow or occluded as illustrated, the visibility state  $s^{(e)}$  from the viewpoint in question is  $\frac{2}{3}$ .

where  $B_\lambda(\lambda, T)$  is the black body spectrum calculated according to Planck's law for temperature  $T$ . Thus, the total power collected in the band  $P|_{\lambda_0+d\lambda}$  is

$$P|_{\lambda_0+d\lambda} = \sum_e \left( P_R^{(e)}|_{\lambda_0+d\lambda} + P_E^{(e)}|_{\lambda_0+d\lambda} \right) \quad (11)$$

### 2.3. Atmospheric effects

Earth's atmosphere absorbs light differently at different wavelengths. Additionally, the amount of atmosphere traversed by light before reaching a sensor directly affects the reduction in signal due to scattering. These two effects must be accounted for in the model. Atmospheric attenuation spectra for the zenith direction were obtained from the MODTRAN software package [21], which gives the fraction of light that reaches ground after traversing the atmosphere. The attenuation spectrum for a zenith-pointing camera can be seen in Fig. 4.

When the telescope points off-zenith at some angle, however, the amount of atmosphere that is traversed by the signal light increases, and so must the atmospheric attenuation. In astronomy, this is captured by the number of 'airmasses' that the signal traverses [22], which as defined as equal to 1 for a zenith-pointing telescope at sea level. The number of airmasses traversed for a given zenith/elevation angle can be approximated with the Kasten and Young 1989 model (see Fig. 5) [23]. The total attenuation is then  $S(\lambda)^{A(\theta_{el})}$ , where  $S(\lambda)$  is the zenith-pointing attenuation spectrum,  $A(\theta_{el})$  is the airmass number corresponding to elevation angle  $\theta_{el}$ . This causes a further reduction to the light collected by the aperture:

$$P|_{\lambda_0+d\lambda} = S(\lambda)^{A(\theta_{el})} \sum_e \left( P_R^{(e)}|_{\lambda_0+d\lambda} + P_E^{(e)}|_{\lambda_0+d\lambda} \right) \quad (12)$$

### 2.4. Sensor model

The sensor was modelled as comprising a single pixel per wavelength band — the collected light is split by a prism or grating onto a single strip of pixels, where their spatial separation allows each pixel to measure the light in that particular wavelength band. This approach was chosen because of the small size of the targeted objects and the large distance at which they will be imaged, making it unlikely for structures to be resolved spatially. Using a 1024-by-1024 array and a 1-degree field of view gives a pixel separation distance of 42 metres at 500 km — far too coarse to resolve objects of size on the order of satellites, even in such a low orbit. For the work in this paper, the wavelength bands chosen were 5 nm wide. Various wavelength ranges were simulated in the simulations in this paper, however in deployment the chosen range of wavelengths will depend on the materials expected to be present in the object being observed, and the wavelengths at which these materials have distinct spectral features. The expected

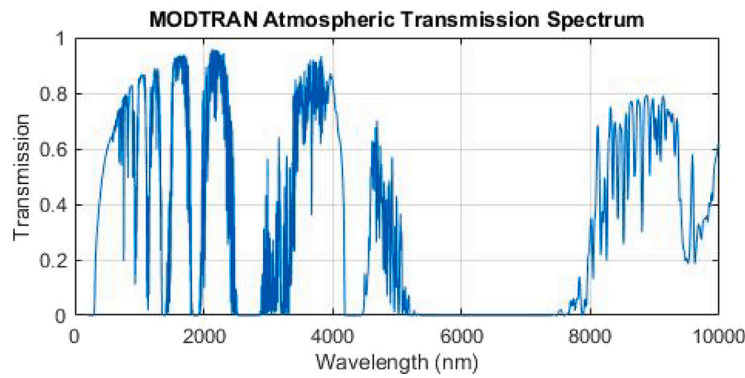


Fig. 4. Atmospheric attenuation spectrum from MODTRAN.

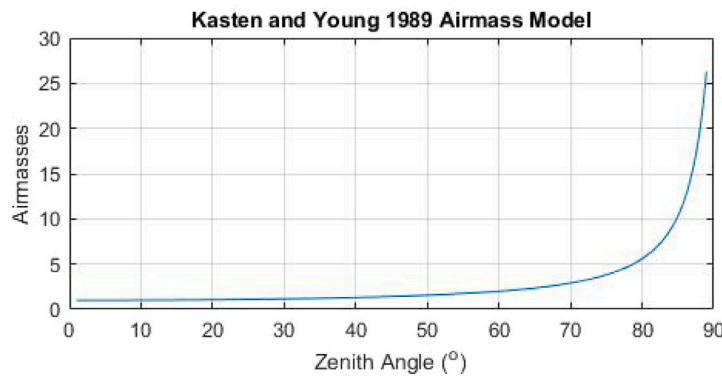


Fig. 5. Kasten/Young model of airmass w.r.t. zenith angle.

photon count in each band is obtained from Eq. (12), and dividing by the photon energy corresponding to the middle of the wavelength band.

Optical efficiency was modelled by an overall efficiency parameter  $\eta_{optics} = 0.5$ , which represents all photon losses from the aperture to the sensor. Sensor noise was modelled as shot noise dominated, and expected photon counts were converted to noisy, simulated photon counts by use of a Poisson random number generator with the expected count in each band as the mean. Thus, the final photon count in the band is

$$n_{ph}|_{\lambda_0}^{\lambda_0+d\lambda} = \mathcal{P}\left(\eta_{optics} \frac{\lambda_0 + \frac{d\lambda}{2}}{hc} P|_{\lambda_0}^{\lambda_0+d\lambda}\right) \quad (13)$$

where  $\mathcal{P}(x)$  denotes a random number generated according to the Poisson distribution with mean value  $x$ ,  $h$  is Planck's constant and  $c$  is the speed of light.

## 2.5. Parametric analyses

To estimate the magnitude of returned signal intensity, test simulations for two cubes of different sizes were performed, for the case of both ground-based and space-based telescopes. These test cases were simulated using conditions close to what is expected in deployment of the system: in the ground case, this means imaging in twilight conditions, i.e. a phase angle of close to 90 degrees, with the object starting its observation arc near the telescope's zenith direction such that atmospheric extinction is minimised. In the orbital observer case, the observer is on a close approach trajectory with slightly different orbital elements, as will be described. The orbit of the target object had semi-major axis 7650 km, eccentricity 0.005 and inclination 23 degrees. The initial true anomaly was 345 degrees, i.e. slightly sunward of the ground station at the beginning of the observation arc. Other orbital elements were zero. For the space-based observer, the

Table 1

Summary of key parameters in the test simulations. Orbital state vectors are written in the standard form for Keplerian elements, with the true anomaly denoting the value at the start of the simulation:  $[a, e, i, \Omega_{RAAN}, \omega_p, \nu_0]$ .

Parameter/property	Value (s)
Cube side length	30 cm, 2 m
Present materials	Steel, aluminium, PVC
Orbital elements (target)	[7650 km, 0.005, 23°, 0, 0, 345°]
Cube rotation rate (random axis)	$\frac{1}{2\pi}$ rads <sup>-1</sup>
Orbital elements (observer)	[7500 km, 0.0003, 10°, 0, 0, 345°]
Telescope latitude	5°
Telescope longitude	0°
Zenith direction	[0.9962 0.0872 0]
Illumination direction	[0 1 0]

semi-major axis was 7500 km, eccentricity 0.0003, inclination 10 degrees, and the remaining orbital elements zero. This led to a close approach on the order of several hundred kilometres from the object. A summary of the key parameters for these tests can be found in Table 1. Material distribution across the cube surface was two opposing faces composed entirely of each of the three materials. More complex material distributions were used in later simulations.

Spectral snapshots for a 30 cm cube can be seen in Figs. 6 to 7, for both ground-based and space-based telescopes, which show the spectral response at a random time during the observation arc in each case. Equivalent results for a larger, 2 m cube in the IR region are shown in Figs. 8 to 9. These examples give an estimate of the power expected to be received by the system in deployment, which informs telescope design. The telescope size for the space cases was chosen to represent cubesat compatible optics (diameter 9 cm), and the ground case was chosen to match that of a telescope available for future experimental work at the Fraunhofer Centre for Applied Photonics (Celestron Edge HD 1400: focal length 391 cm, diameter 35.6 cm).



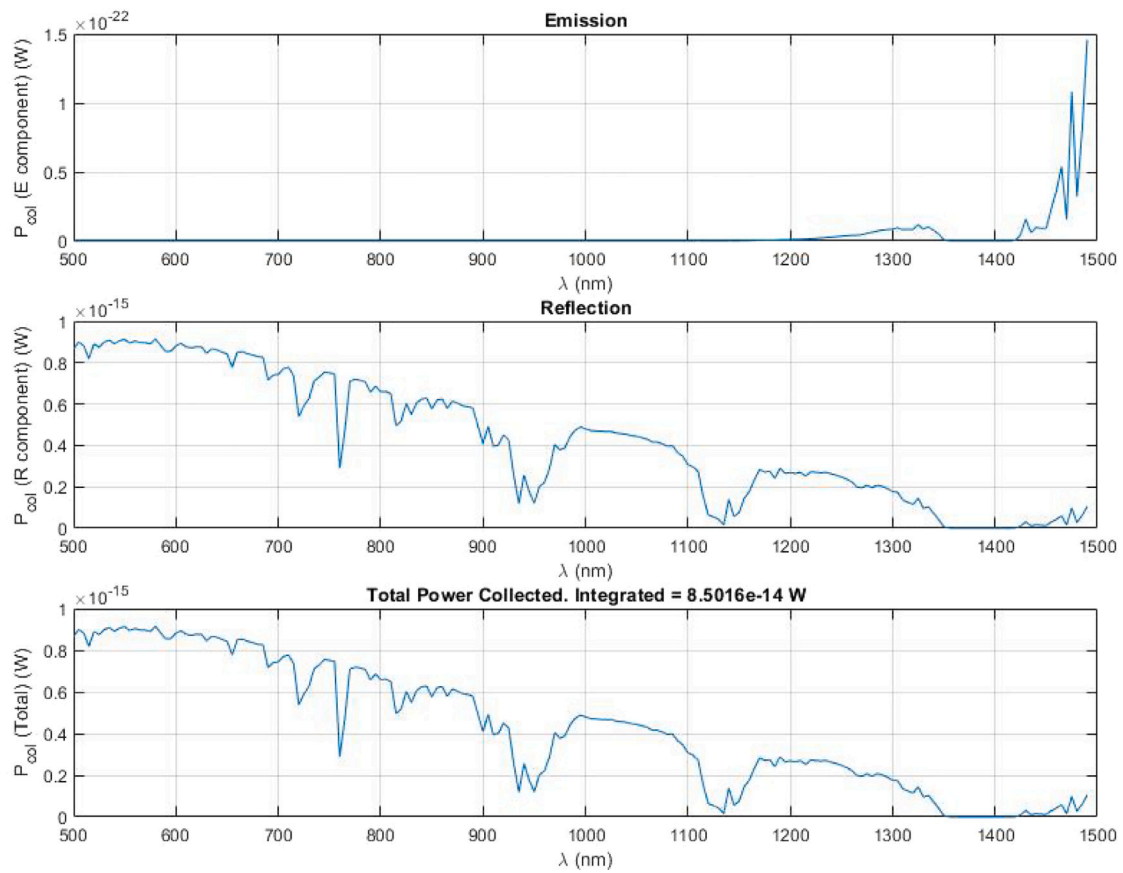


Fig. 6. Simulated signal from a ground-based telescope with radius 17.8 cm observing a 30 cm cube in visible/near infrared.

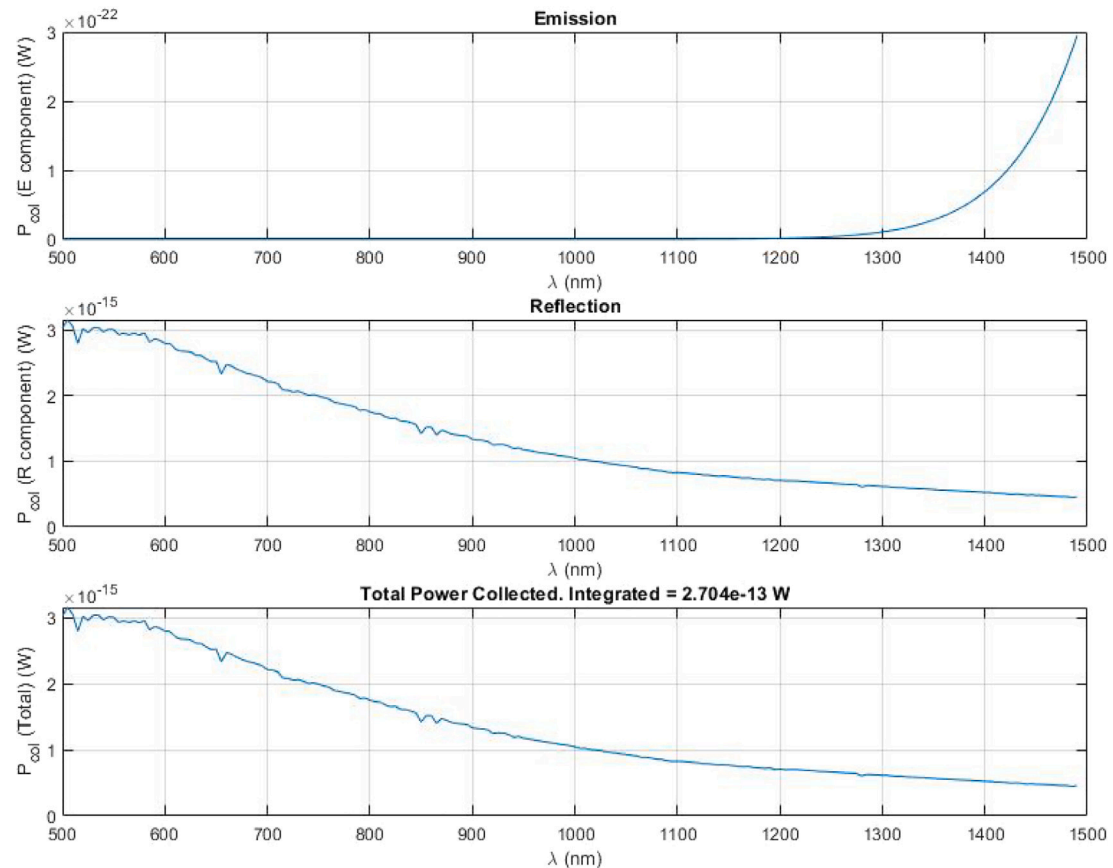


Fig. 7. Simulated signal from a satellite-mounted telescope with radius 4.5 cm observing a 30 cm cube in visible/near infrared.

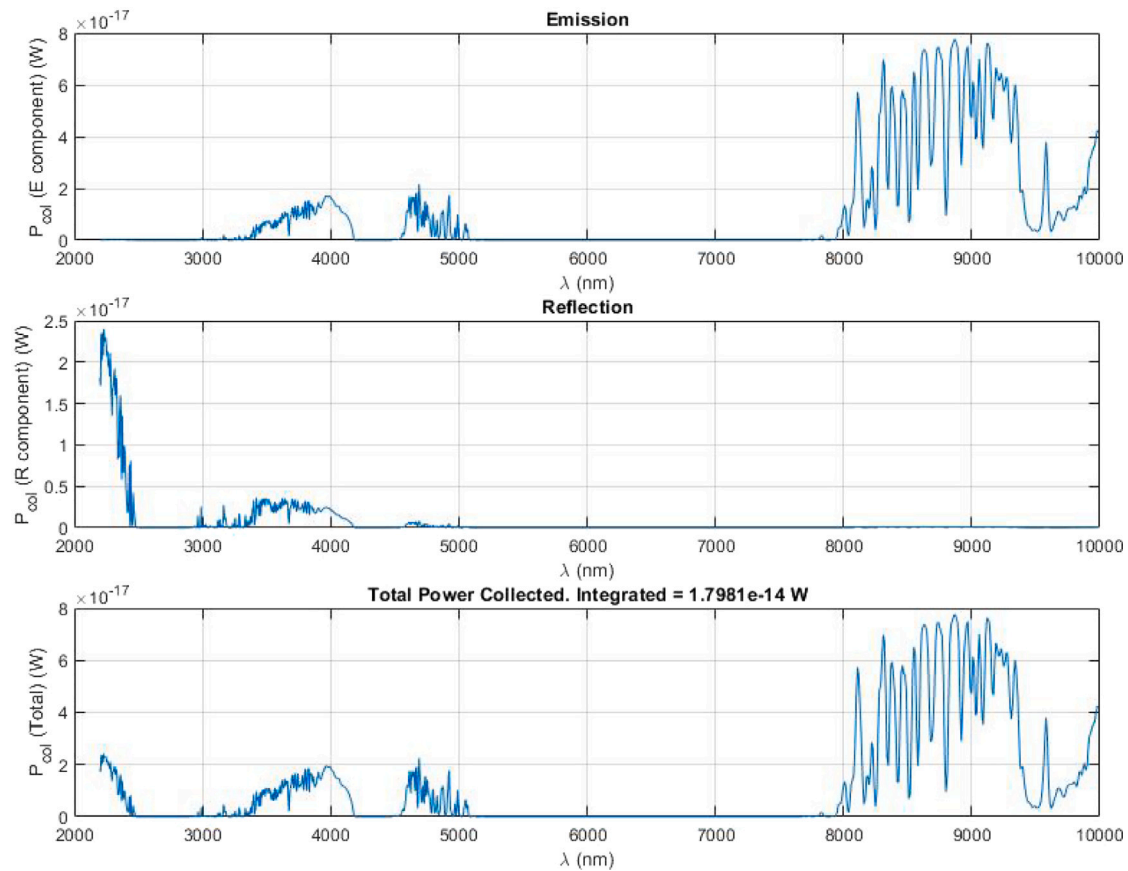


Fig. 8. Simulated signal from a ground-based telescope with radius 17.8 cm observing a 2 m cube in infrared.

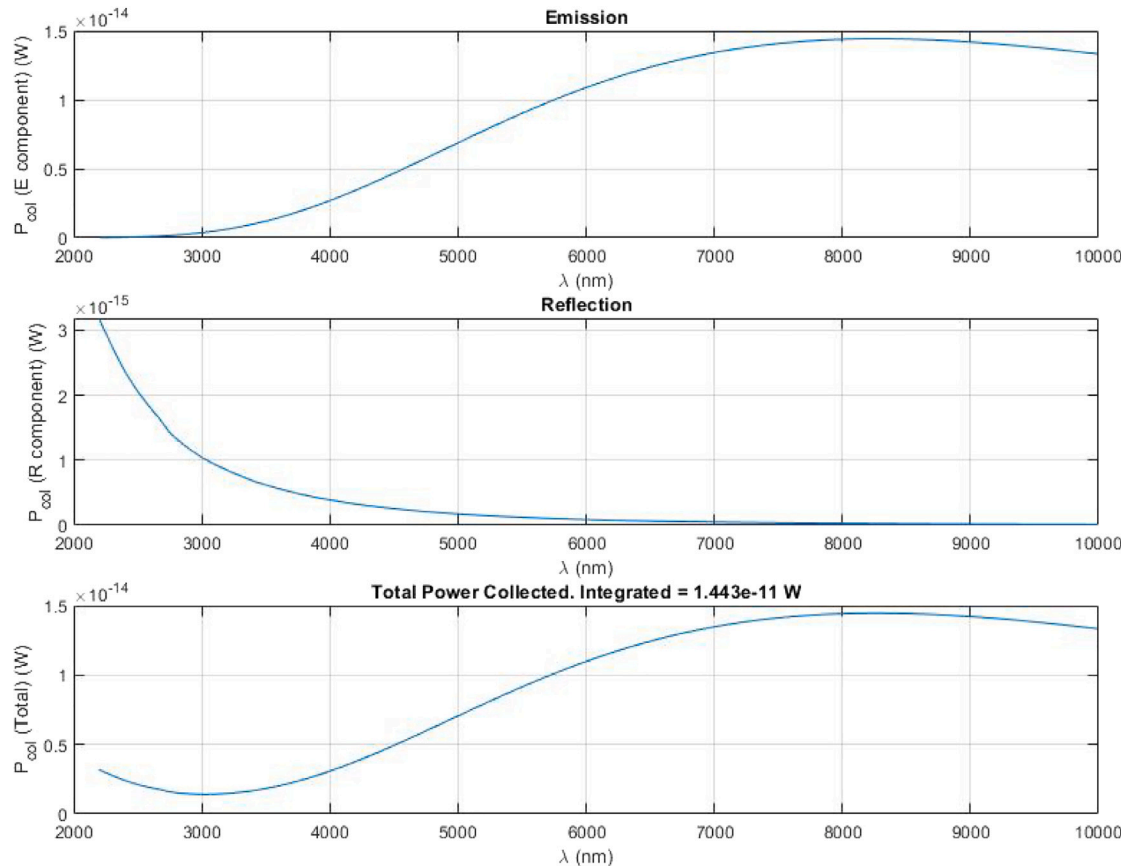


Fig. 9. Simulated signal from a satellite-mounted telescope with radius 4.5 cm observing a 2 m cube in infrared.

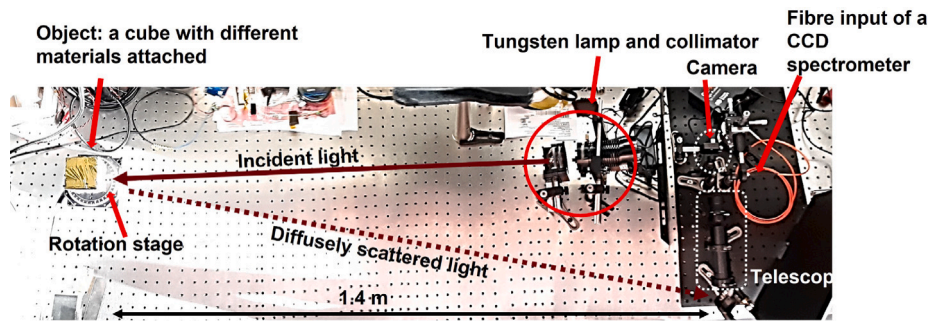


Fig. 10. The lab prototype of the hyperspectral surveillance system assembled in Fraunhofer-CAP.

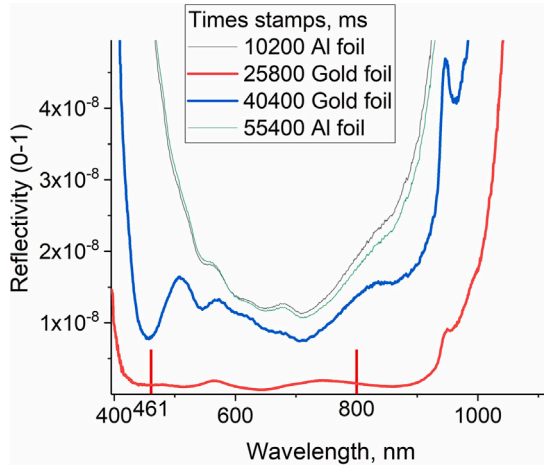


Fig. 11. Characteristic reflectivity spectra of Al and gold foil measured using the setup shown in Fig. 10. The spectra are shown for different time from the start of experiment (time stamps), which correspond to different rotation angle of the cube. Timestamps corresponding to the maximum signal in the spectrometer were chosen.

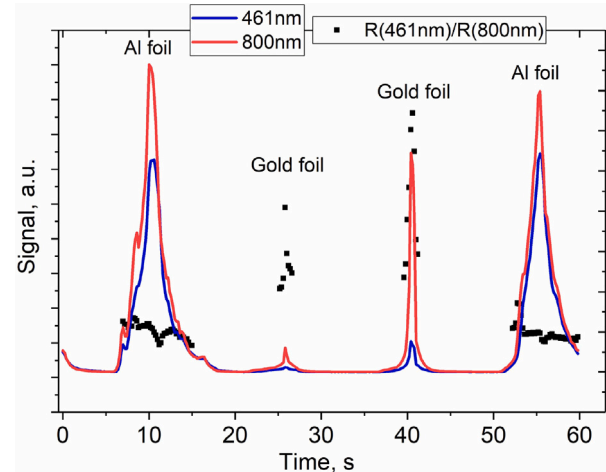


Fig. 12. The ratio of reflectivity of Al and gold foil at the wavelengths of 461 and 800 nm (squares) as a function of rotation time. Solid lines represent the actual signal at these two wavelengths recorded by the spectrometer. The ratio is shown only at the time stamps corresponding to max signal at these two wavelengths, otherwise the signal-to-noise ratio is too small.

However, larger telescopes may be desirable in the ground-based case to better leverage the lack of size and mass restrictions inherent in ground-based operation compared with space-based operation.

### 3. Experimental testing

A proof-of-concept hyperspectral telescope was designed and assembled by the Fraunhofer Centre for Applied Photonics. This lab-based system comprises a telescope, a camera for object visualisation and an off-the-shelf spectrometer (Fig. 10). A cube with various materials (aluminium, Al, glass, gold foil, Teflon, white enamel, titanium) attached to its surfaces was used as the object. The object was positioned on the motorised rotation stage. It was illuminated by a tungsten-halogen lamp. Reflected light collected by the telescope was split into 2 channels: visualisation, with a CCD camera, and measurement, with the monochromator for temporal analysis of the spectral response from the object.

Some preliminary experimental results were obtained with this setup. The cube was covered with Al and gold foil. It was rotated with the speed of 6 degrees per second. Reflectivity spectra of surfaces were recorded by the spectrometer. The characteristic reflectivity spectra of Al and gold foil corresponding to the maximum signal on the spectrometer at certain times (the so-called time stamps) are shown in Fig. 11.

One can pick up two characteristic wavelengths in these spectra, where a significant difference in the ratio of reflectivity coefficients between Al and gold was observed: 461 nm and 800 nm. The wavelength of 461 nm corresponds to a dip in the reflectivity spectrum of gold

foil and 800 nm corresponds to a shoulder in the reflectivity spectrum of gold foil, while no specific features are observed in the reflectivity spectrum of Al foil at these two wavelengths. The ratio of reflectivity coefficients at 461 and 800 nm was plotted as a function of time in Fig. 12 (black squares), together with the actual reflectivity values at these two wavelengths (solid lines).

Analysis of the ratio of the reflectivity coefficients as a function of time at specific wavelengths can provide some information about the material the object of observation is made of. These test results confirmed the hypothesis that by looking at the spectral signature we could identify the combination of materials presented to the camera. Since the hyperspectral imager gives us the full range of intensities at different wavelengths, in the following the intensity over a wide range of wavelengths will be considered to identify materials and material mixtures through a process of spectral unmixing.

#### 3.1. Unified reflection model and laboratory test validation

The model used to test the endmember decomposition and the attitude estimation was based on a simple Lambertian surface hypothesis. While for some materials this is a good approximation, for others such as glass, polished metal etc. it is important to also model the specular components of the reflected light. Additionally, for materials with a complex refractive index (metals, dielectrics), the Fresnel equations predict a reflectance fraction that varies not only in wavelength, but also in the angle of incidence to the surface. Thus, we also implemented the model presented in [24]. This model unlike many in the field of

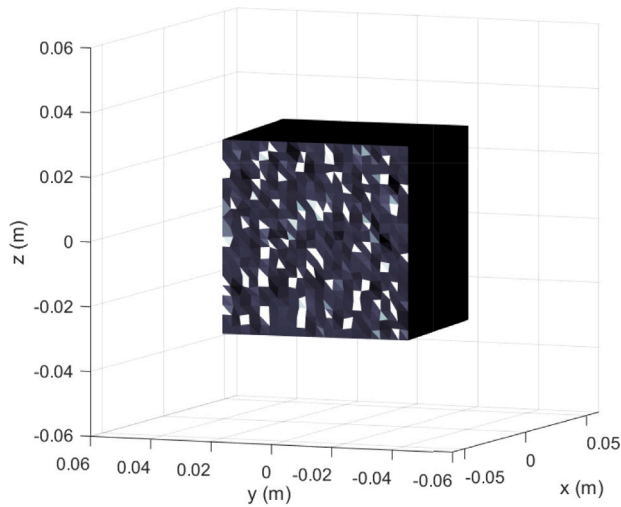


**Fig. 13.** Unified reflection model applied to crinkled foil surface, modelled by non-flat foil with low roughness. Brighter regions indicate more reflected light from those elements.

computer graphics is physically-based, and does not require the use of a physically meaningless and arbitrarily-chosen ‘specular fraction’ which dictates the proportion of light that is reflected specularly vs diffusely. The model is based on the common microfacet model of rough surfaces, whereby a macroscopically flat but rough surface is represented by a collection of specularly-reflecting microfacets whose

orientation relative to the local macro normal vector follows some statistical distribution. Specular reflection from individual microfacets is governed by the Fresnel equations. The only required inputs for this model are the complex refractive index of the material, its surface roughness parameter  $\nu$  (RMS slope of the microfacets), and its ‘intrinsic reflectivity’, i.e. the proportion of absorbed light predicted by the Fresnel equation which is then scattered by the first few atomic layers of the surface and exits again — effectively Lambertian reflectance.

Although the original paper on this model contained validation against some materials, the materials expected to be encountered in space objects may be quite different from the macroscopically flat surfaces. For example, crinkled thermal blankets clearly occupy an intermediate regime of being microscopically smooth (low surface roughness), however macroscopically there are relatively large, millimetre-scale bumps and imperfections. It is unclear how such materials should be best modelled, since these surface features may be too large to treat statistically by use of a high roughness parameter. In order to determine how to best model such materials, we compared two modelling techniques with lab data. The first method treats the crinkled foil as flat, with a high roughness parameter  $\nu = 0.15$ . The second method involves refinement of the mesh and the addition of noise to vertex locations in 3D space. This creates a surface with many imperfections as can be seen in Fig. 13 which approximates the real foil surface. The roughness parameter in this case is set to a lower value of  $\nu = 0.06$ , corresponding to a microscopically smooth, reflective surface.

A laboratory setup was designed to collect data for the model validation. Here we had a cube placed on a rotation stage, with different materials on each face, illuminated obliquely with a tungsten lamp and diffuser. For testing a thermal blanket analogue, one side of the cube was covered with crinkled aluminium foil, and the rest with black paint.

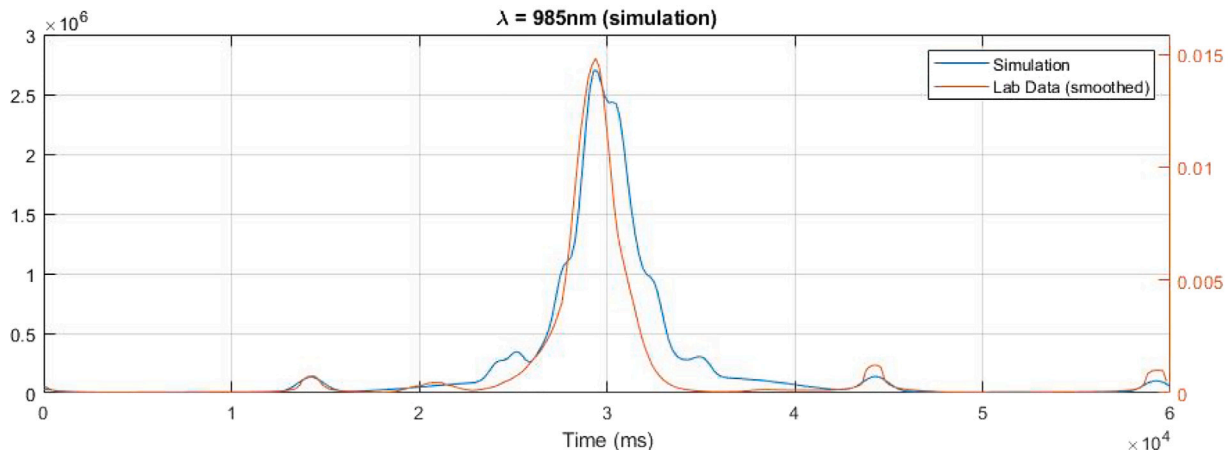


**Fig. 14.** Comparison of simulated measurements and lab measurements for rotating cube at 985 nm, using non-flat, low roughness foil approximation ( $\nu = 0.06$ ).

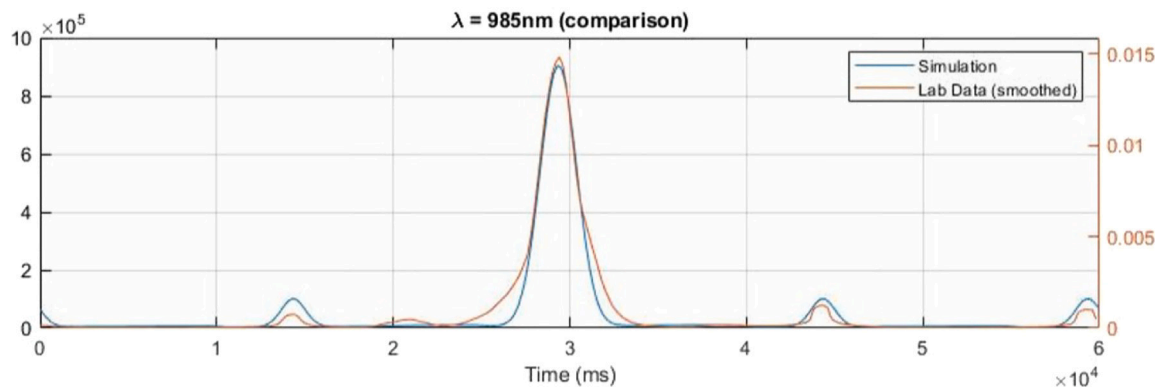


**Fig. 15.** Comparison of simulated measurements and lab measurements for rotating cube at 985 nm, using flat, high roughness foil approximation ( $\nu = 0.15$ ).



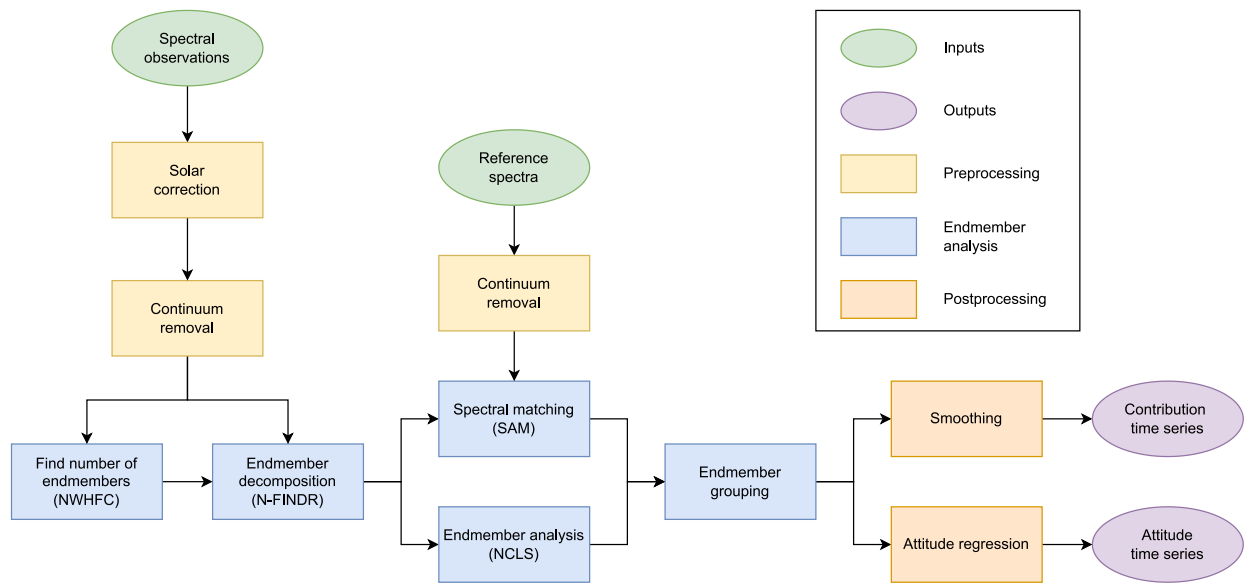


Fig. 16. Block diagram of material contribution analysis method. Contribution time series data can also be used for attitude estimation.

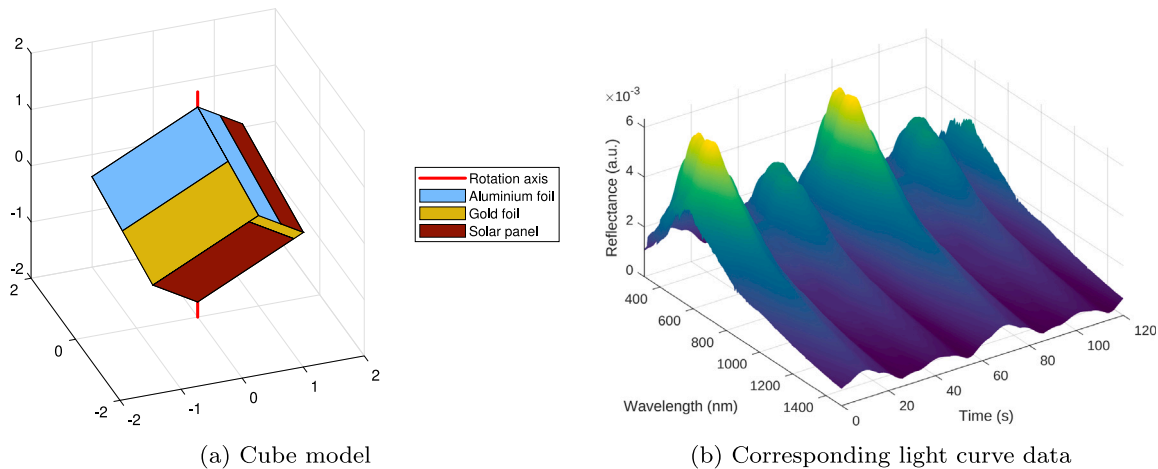


Fig. 17. Spectral light curve for a simulated test cube rotating at 1 rpm, with faces consisting of a mixture of three materials (aluminium foil, gold foil and solar panels).

The cube was set to rotate under a fixed point of the spectrometer camera, which collected spectra from the object at 200 ms intervals as it rotated. Light was collected from a small circular area in the centre of the camera's field of view, through which the cube surfaces passed. This lab scenario was simulated using the previously mentioned model, by updating the rotation state of the cube at each time step, and matching all physical dimensions, angles and distances. Refractive index data for thin film aluminium oxide was used as the input in this case, since the validation is being carried out in an oxygenated environment and bare aluminium is not the reality of the sample being used. In the lab measurements, one full rotation of the cube was measured, resulting in small specular peaks for each painted face, and one much larger peak due to the foil side.

The results of the two methods superimposed on the smoothed lab data at an arbitrarily chosen wavelength can be seen in Figs. 14 to 15. Although both provide a reasonable approximation of the light curve of the rotating foil face, the high roughness method appears to be a better model. Since this method requires fewer polygons in the 3D model, the simulation is also significantly faster. For these reasons, we conclude that crinkled foil surfaces should be modelled as flat, with high roughness, rather than non-flat with low roughness.

#### 4. Spectral light curve analysis

The aim of the spectral analysis is to obtain the contribution of spectrally distinct materials to the spectrum received by the sensor. The unmixed contribution of each material together with information about the illumination source will be used to construct a model of the object and deduce the pointing direction of its surfaces.

The proposed spectral analysis process progresses through a number of steps, summarised in Fig. 16. As an illustrative example of the process in Fig. 16, Fig. 17 shows the light curve for a test cube, simulated with the model described in the previous section, with surfaces consisting of three materials, rotating about a fixed axis passing through opposing corners. The distribution of materials across the six faces are shown in Table 2. In the table, the axes indicated in the first column correspond to the six faces of the cube, notated in the body frame. A complex distribution of materials was chosen to verify that the unmixing (endmember decomposition in the following) would be capable of extracting material spectra even when some materials are not isolated (100% contribution to signal) at any time point in the integration.

These simulations were performed under simulated laboratory conditions, as a proof of concept - i.e. using fixed-axis rotation and an

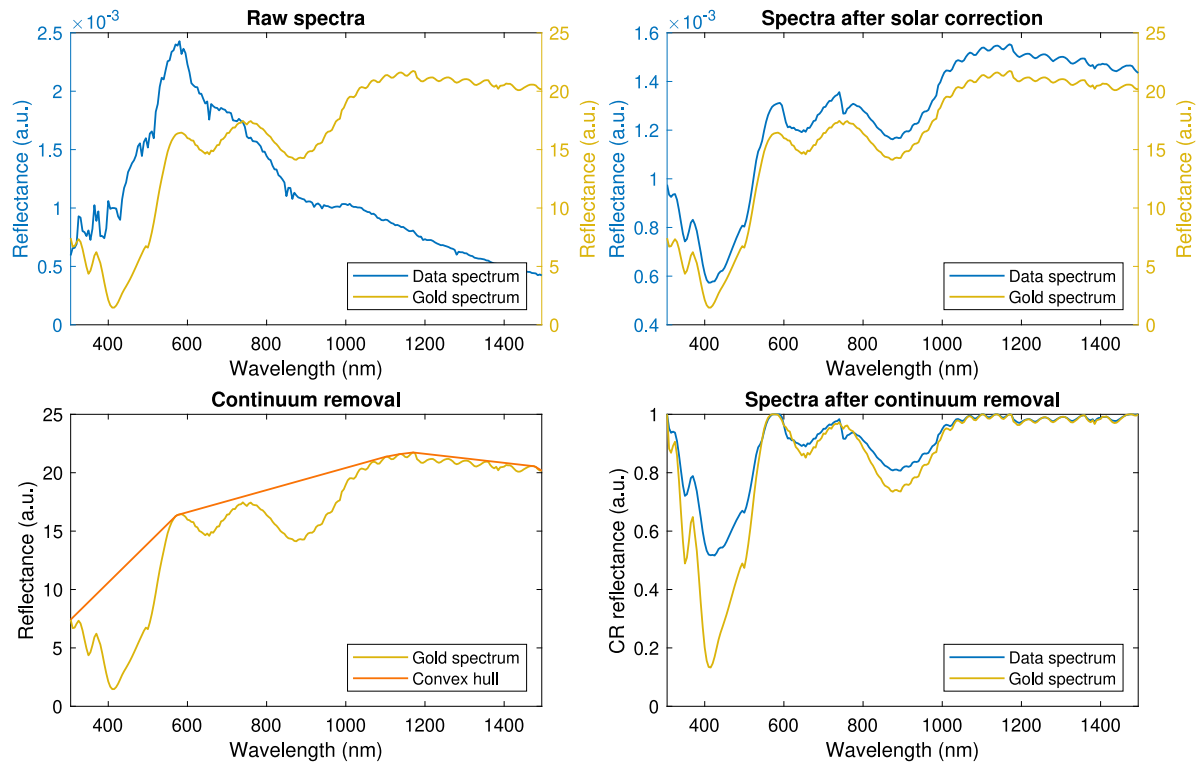


**Fig. 18.** Preprocessing steps applied to a simulated spectrum taken from the test object represented in Fig. 17 and a reference spectrum for gold material. Spectra are first normalised to the mean solar spectrum, and then further normalised using continuum removal, which is achieved by dividing each point of the spectrum by the point on the line that forms a convex hull over the top of the spectral curve.

**Table 2**

Abundances of each material for the first test cube. Material spectra collected in lab experiments.

Cube face (body axis)	Aluminium foil fraction	Gold foil fraction	Solar panel fraction
+x	0.5	0	0.5
+y	0	0	1
+z	0.5	0.5	0
-x	0.75	0	0.25
-y	0	0.135	0.865
-z	0	0.5	0.5

object whose centre of mass does not move with respect to the observer. The camera was simulated to be looking toward the cube along the positive  $x$  axis, at a distance of 0.5 metres, thus the unit vector in the view direction is  $\hat{\mathbf{V}} = [1, 0, 0]^T$ . The illumination direction  $\hat{\mathbf{S}}$  was chosen to be behind the observer, i.e.  $\hat{\mathbf{S}} = \hat{\mathbf{V}}$ . The MODTRAN extraterrestrial solar spectrum (corresponding to the intensity at 1 astronomical unit) was used as the illumination source. Cube side length was 6 centimetres and aligned such that the  $z$  axis (also the constant axis of rotation) was aligned with two opposing corners, such that all faces are visible to the camera at some point in a full revolution.

The data is preprocessed in two stages, as shown in Fig. 18. The solar illumination is corrected for by dividing each sample of the data by the mean solar spectrum, after which continuum removal is performed on both the data and the reference spectra, in order to normalise the spectra and remove any deviating baselines.

After preprocessing, endmember decomposition is performed using the N-FINDR algorithm, which maximises the volume of a simplex with endmember spectra at the corners [25]. This results in a collection of  $N$  endmember spectra, which are candidate spectra that should correspond to individual materials present on the surface of the object. As  $N$  is an input to N-FINDR, an estimate for the number of

candidate spectra must first be determined. One option is to use a noise-whitened Harsanyi–Farrand–Chang (HFC) algorithm [26,27], which will be discussed in more detail in Section 4.1. Endmember analysis, using non-negative constrained least-squares regression (NCLS), then determines the relative contribution of each endmember to the overall spectrum for each point in time [28]. This is analogous to abundance estimation in conventional 2-dimensional hyperspectral scenes.

Fig. 19 shows the results of applying this analysis to the simulated cube. The ground truth contribution curves represent the fraction of the object facing the observer that is composed of each material. As not all of this area is evenly illuminated, the relative contributions estimated using NCLS are not accurate; however, the peaks of these curves correlate closely with the peaks in the ground truth curves.

Classification of the endmembers is performed using spectral matching, with reference to known spectra of common materials from a spectral library. Spectral matching uses the Spectral Angle Mapper (SAM) algorithm [29], shown in Fig. 20(a). The SAM score  $\alpha$  is defined as:

$$\alpha = \cos^{-1} \left( \frac{\sum_{i=1}^n X_i R_i}{\sqrt{\sum_{i=1}^n X_i^2} \sqrt{\sum_{i=1}^n R_i^2}} \right), \quad (14)$$

where  $X_i$  is the  $i$ th band of endmember spectrum  $\mathbf{X}$ ,  $R_i$  is the  $i$ th band of reference spectrum  $\mathbf{R}$ , and  $n$  is the number of spectral bands. Lower SAM scores indicate greater spectral similarity. This calculation is performed for each pair of endmember/reference spectra, and the endmember is assigned to the material with the lowest score. Fig. 20(b) shows the results of applying this classification to the endmembers obtained for the simulated cube. The result is a time series of the relative contribution of each known material. Smoothing is applied to obtain the final contribution time series data, using a Gaussian filter with a window size of 3 samples. Finally, the contributions curves are normalised to sum to 1 at each point in time, so that they represent the relative contributions of the materials.

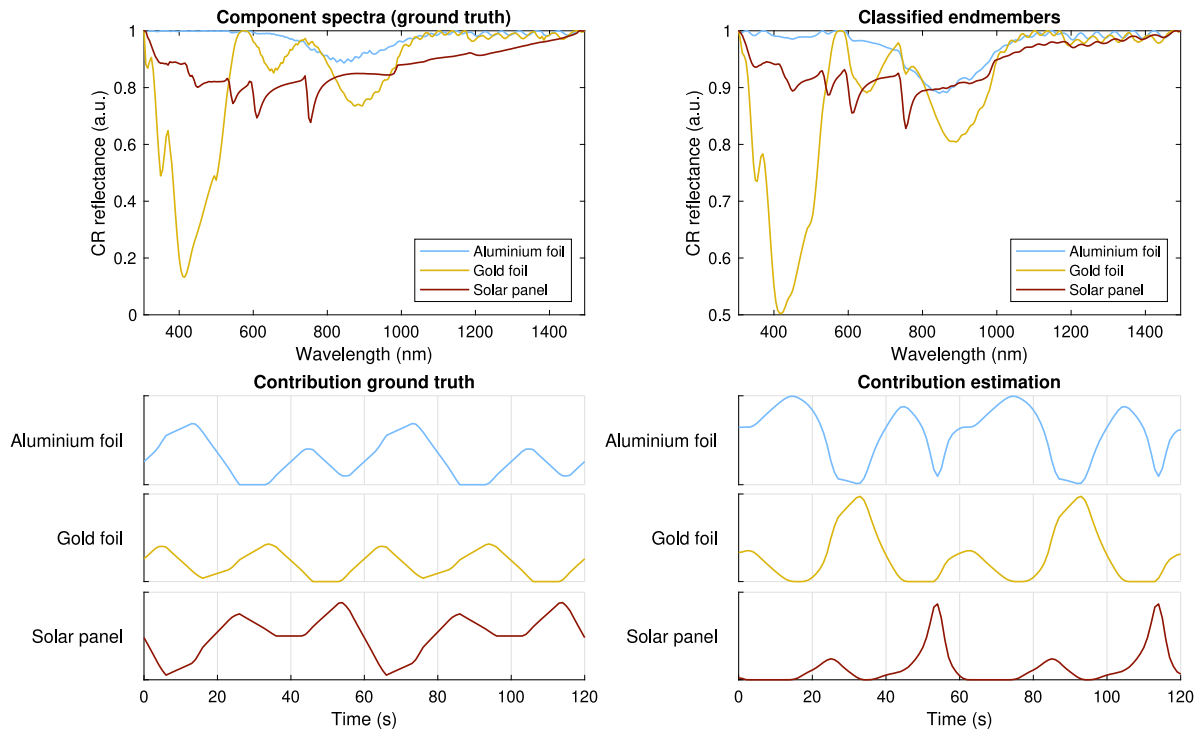


Fig. 19. Initial results for a cube-shaped test object. In the top row, the extracted endmember spectra are presented in comparison to the ground truth spectra. Fig. 20(b) shows the SAM scores used to classify the endmembers. The bottom row presents the corresponding smoothed contribution time series curves, extracted using the NCLS method. Although the relative contributions are not always accurate due to illumination conditions, the peaks in the estimated contribution curves correlate closely with the peaks in the ground truth curves obtained from the model.

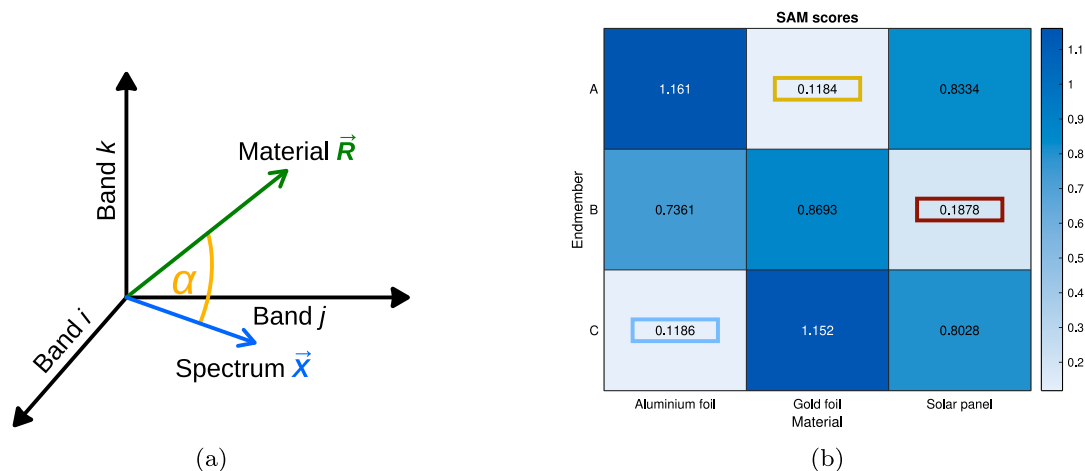


Fig. 20. The Spectral Angle Mapper (SAM) algorithm measures the angular distance  $\alpha$  between the bands of two spectra. Applying this method to each pair of endmember/reference spectra from the cube simulation results in the heatmap in (b), with the lowest score in each row highlighted. Lower scores indicate greater spectral similarity. Using these scores, endmembers A, B, and C can be assigned to the gold foil, solar panel, and aluminium foil classes, respectively.

Fig. 21 demonstrates the advantages of using contribution curves for attitude estimation over a panchromatic light curve. Not only are peaks in the frequency domain more pronounced using the contribution data, but differences in the peaks between contribution curves for separate materials are indicative of faces with different material compositions, making it feasible to correct for harmonics in the frequency domain caused by object symmetry.

#### 4.1. Estimation of the number of materials

One significant limitation of the N-FINDR algorithm is its reliance on prior knowledge about the ground truth number of materials  $N_{GT}$  present in the scene. Fig. 22 shows the effects of using an incorrect

value  $N$  to guess  $N_{GT}$ . When  $N < N_{GT}$ , two or more materials may be combined in a single endmember, or less dominant materials may be omitted altogether. In a situation in which specific materials are sought, this is not a limitation. If  $N > N_{GT}$ , some materials will have shadow spectra. In this case, material classification will result in multiple materials associated to the same endmember. Once they have been identified using SAM, these endmembers may be combined into a single spectrum prior to contribution analysis. For this reason, it is generally preferable to overestimate the value of  $N$  than to underestimate it.

In practice, the correct value of  $N$  is unlikely to be known a priori, so an algorithm is required to determine the value from the available data. An option is to use the noise-whitened HFC (NWHFC) algorithm to estimate the number of endmembers present in the scene [26]. NWHFC

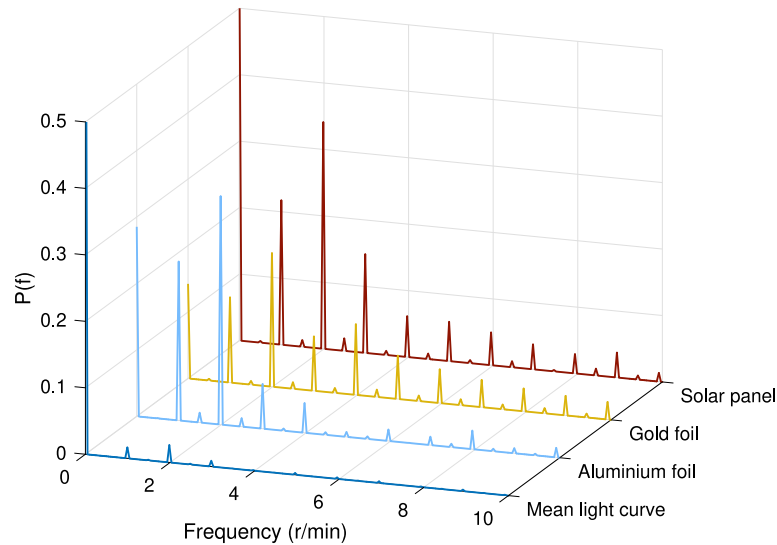


**Fig. 21.** Fast Fourier transform (FFT) of the mean light curve data compared with each of the contribution curves. Differences between the heights of the peaks in these frequency domain curves (such as the relatively higher peak in gold foil at 4 rpm) can be leveraged to obtain additional information about the object's rotation.

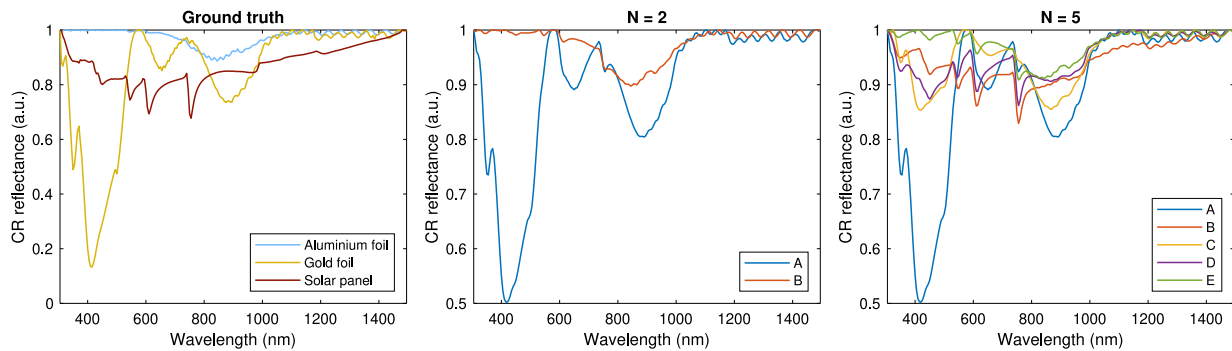


**Fig. 22.** Comparison of results using the incorrect number of endmembers as an input to the N-FINDR algorithm. When  $N < N_{GT}$ , as in the middle pane ( $N = 2$ ), endmembers will comprise features of multiple ground truth materials. Note that endmember A in this example is similar to the gold foil spectrum, and B is similar to the aluminium spectrum, but both endmembers also contain features of the solar panel spectrum, such as a narrow absorbance band at around 680 nm. When  $N > N_{GT}$ , as in the right pane ( $N = 5$ ), multiple endmembers are found for some ground truth materials. In this case, endmembers A and C are representative of gold foil, and B and D are representative of solar panels.

estimates the virtual dimensionality (VD) of the signal, a measure that represents the number of spectrally distinct signal sources, by comparing the eigenvalues of the correlation matrix and the covariance matrix of the signal. For a noise component, these values will be the same. Therefore, the VD can be estimated as the number of spectral components for which the difference between the eigenvalues is above some small threshold value. The sensitivity of the algorithm can be adjusted using the probability of false alarm (PFA) parameter, which controls this threshold value.

NWHFC performs best when the number of hyperpixels  $s$  is significantly higher than the number of bands  $n$ . For time series consisting of few sample points, the number of endmembers is significantly overestimated. One approach to solving this problem is to artificially augment the data available during this stage by adding Gaussian noise to repeated copies of the input data. In our test case, consisting of 121 samples, three repetitions of the input data were sufficient to overcome the lack of a sufficient number of hyperpixels. The number of endmembers may still be underestimated in cases where multiple materials have similar spectral signatures. For this reason, larger quantities of source data are still preferred for greater reliability. Increasing the PFA parameter may significantly alleviate this problem, as shown in Fig. 23, but comes at the expense of an increased risk of false positives. The number of false positives varies depending on numerous factors, including the signal-to-noise ratio; for this reason, it is necessary to revisit the tuning of this parameter when working on new datasets.

**Table 3**

Material distribution of the full pipeline simulation.

Cube face (body axis)	Steel fraction	Aluminium fraction	PVC fraction
+x	0	0.5	0.5
+y	0	0	1
+z	0.5	0	0.5
−x	0	1	0
−y	0	0	1
−z	0.5	0.5	0

A new case was simulated to test the full pipeline of sensor simulation – endmember decomposition – attitude estimation, using a different cube-shaped object with the material distribution shown in Table 3. As well as the simulated hyperspectral imager signal, the sensor simulation also outputs the ground truth of the material contribution curves — the fraction of the object's projection onto the image plane that is composed of each constituent material.

Conditions for the simulations in this case were the same as for the previous case, except for a different illumination vector  $\hat{S} = [0.0995, 0.995, 0]^T$ , i.e. a phase angle of just less than 90 degrees. Additionally, the cube's body-frame +z axis/face is aligned with the inertial +z axis rather than rotating about an axis passing through opposing corners. The cube is again fixed-axis rotating at 1 revolution per minute.



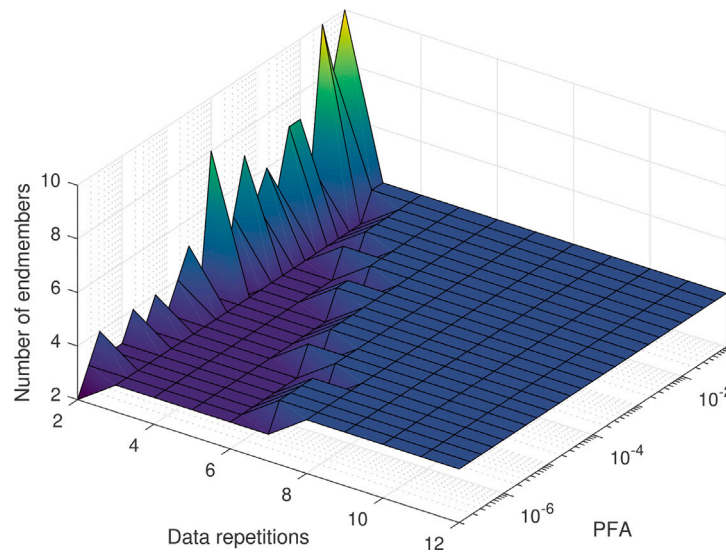


**Fig. 23.** Number of endmembers predicted by the NWHFC algorithm for the simulated cube, which has 121 samples points across 239 bands. Without data augmentation, there are too few sample points to obtain a reasonable estimate (the predicted value for one repetition is in the region of 60–120). For small numbers of repetitions, the value is underestimated, as one of the spectral components has a flat profile that is difficult to detect. For large numbers of repetitions, the correct result is obtained. Increasing the probability of false alarm (PFA) lowers the number of repetitions required to achieve the correct result; however, this also significantly increases the risk of false positives in noisy data.

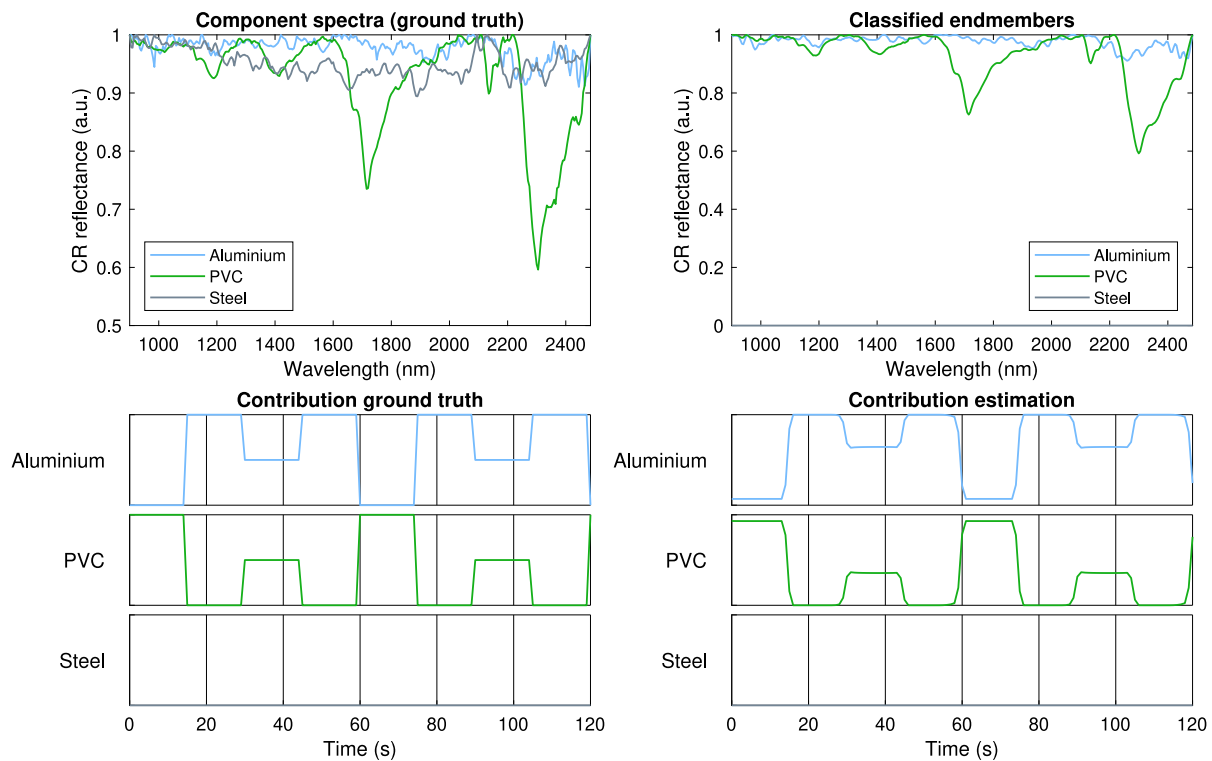


**Fig. 24.** Spectra recovered from endmember decomposition compared to the true spectra. Since steel was not present on the object, no corresponding endmember was identified. Beneath that, the contribution estimation determined by endmember analysis is shown. As in the other example, the overall shape of each curve closely resembles the ground truth, but the relative contributions at each point in time contains inaccuracies resulting from illumination conditions (e.g. from 30–42 s, the proportion of PVC relative to aluminium is underestimated).

Fig. 24 shows the decomposed spectra and contribution curves for this test case. The large phase angle in this case combined with the different orientation of the rotation axis with respect to the body frame causes a much more rapid transition between materials in Fig. 24 compared with the more gradual transitions in Fig. 19. Since the cube rotates about  $+z$  and the view direction is along the inertial  $+x$ , only Aluminium and PVC are visible during the simulation. The endmember decomposition successfully recovered two spectra which matched the

input spectra of aluminium and PVC, as well as abundance curves which match well with the ground truth (see Fig. 24).

In Fig. 24 one can see the normalised relative abundance of materials in view. The view from the camera at four discrete points in time is shown in Fig. 25. From this plot, one can see that there are two different combinations of materials that periodically come in view, with one of the two with double the frequency of the others. This suggests four different faces with a mix of Aluminium and PVC.

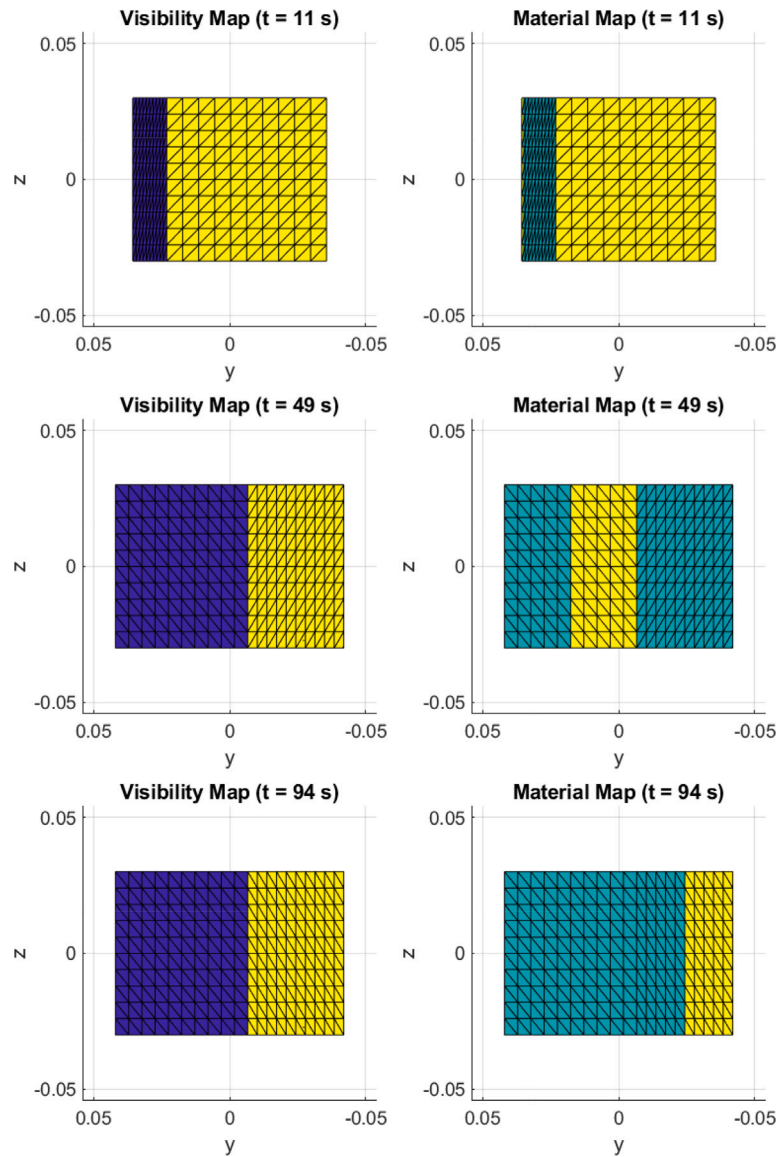


Fig. 25. Cube as viewed from sensor location at various times, illustrating material distribution and visible elements. Illumination vector is  $[0.0995, 0.995, 0]^T$ , i.e. phase angle close to 90 degrees. On the material maps, cyan corresponds to aluminium, and yellow to PVC. Steel is present only on the top and bottom faces, which are out of view. (For interpretation of the references to colour in this figure legend, the reader is referred to the web version of this article.)

## 5. Attitude estimation

Once the time series of the spectra are received and unmixed, one can associate the spectral response of each surface to a particular attitude. In this section, we investigate two conceptually different approaches. In the first approach, we try to identify the pointing direction of a particular combination of materials that we associate to a virtual face with a corresponding normal vector  $\hat{\mathbf{n}}$ . Thus, we exploit the unmixing and attempt an association of endmembers to surfaces. In the second approach, we start directly from the mixed spectra and associate their time series to the time series of the corresponding quaternions through a machine learning model.

### 5.1. Estimation with least square regression

Under the assumption that the object we are observing is equivalent to a cube with six faces, what we call an eCube, and assuming that the unit observation vector (observer to object direction)  $\hat{\mathbf{V}}$  and illumination vector (illuminator to object direction)  $\hat{\mathbf{S}}$  are known we can build

the following simple observation model:

$$\mathbf{y}(\lambda) = \sum_{i=1}^6 \max(0, -\hat{\mathbf{S}} \cdot \hat{\mathbf{n}}_i) \max(0, -\hat{\mathbf{V}} \cdot \hat{\mathbf{n}}_i) \mathbf{F}_i \circ \mathbf{R}(\lambda) \quad (15)$$

where  $\mathbf{y}(\lambda)$  is an  $m$ -element vector containing the  $m$  material-wise contributions at wavelength  $\lambda$ ,  $\hat{\mathbf{n}}_i$  is the normal vector of face  $i$ ,  $\mathbf{F}_i$  is the  $i$ th column of an  $m \times 6$  matrix  $\mathbf{F}$  containing the fractions (normalised to 1) of detected materials on an e-face coming from the endmember analysis,  $\mathbf{R}(\lambda)$  is an  $m \times 1$  vector containing the reference spectra of each material. Thus, the Hadamard product of  $\mathbf{F}_i$  and  $\mathbf{R}(\lambda)$  gives the reference intensity due to each material. We can now look for the global minimiser of the following cost function:

$$J(\mathbf{n}) = \sum_k \sum_j (T_j(\lambda_k) - \sum_i y_{ij}(\mathbf{n}))^2 \quad (16)$$

which is minimised with respect to the pointing direction of one of the eCube faces only,  $\hat{\mathbf{n}}$ . Since the other 5 are rigidly attached, aligning one face correctly is sufficient to recover the rotation state of the eCube. Here,  $T(\lambda)$  is the measured intensity per identified material at a given wavelength  $\lambda$ , which we sum over a number of wavelengths and  $m$

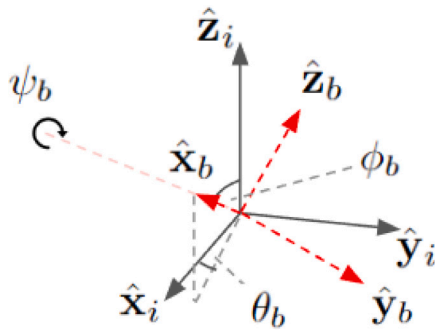


**Fig. 26.** Definition of angles used in the attitude cost function. eCube attitude is defined by three angles,  $\theta_b$ ,  $\phi_b$  and  $\psi_b$ .  $\theta_b$  and  $\phi_b$  are the azimuth and elevation of the  $+x$  face normal with respect to the inertial frame ( $\hat{x}_i, \hat{y}_i, \hat{z}_i$ ), and  $\psi_b$  is the rotation of the other two body axes about the  $+x$  face normal  $\hat{x}_b$ . Here the body frame unit vectors  $\hat{x}_b, \hat{y}_b, \hat{z}_b$  are aligned with the  $+x, +y$  and  $+z$  faces respectively.  $\theta_b, \phi_b, \psi_b$  equal to zero implies the body axes are aligned with the inertial axes.

materials. As a first experiment, we minimise the cost function  $J$  with respect to the angles  $\theta$  and  $\phi$  defining the azimuth and elevation of the  $+x$  face normal of the eCube  $\mathbf{n}_1$  with respect to the inertial reference frame in which  $\hat{\mathbf{V}}$  and  $\hat{\mathbf{S}}$  are defined, as illustrated in Fig. 26.

The global minimum is sought by using a multi-start procedure combining Latin hypercube sampling with the Matlab `fmincon` function. The cost function  $J$  often has a complex landscape depending on the material distribution and illumination conditions, but in some cases it presents a nice shape with clear minima.

Fig. 27 shows an example corresponding to the case depicted in Fig. 17, with a cube rotating around the  $z$  axis. Here, the simulation was performed for the same lab conditions as the pipeline test, with the illumination vector  $\hat{\mathbf{S}} = [0.7071, 0.7071, 0]^T$  giving a phase angle of 45 degrees. We consider the normal to the face initially pointing in the  $+x$  direction and assume a rotation of 32 degrees around  $z$ . This would correspond to a  $\theta_b$  angle of 32 degrees,  $\phi_b = 90$  degrees and  $\psi_b = 0$ . Fig. 27 on the right shows the landscape of  $J$  for this configuration. The global minimum is correctly identified at  $\theta_b = 32$  and  $\phi_b = 90$ .

These two angles are not sufficient to account for all rotations. Thus, we introduce a further rotation angle  $\psi_b$  around the normal vector  $\mathbf{n}$ . Thus, the solution needs to globally minimise  $J$ , with respect to  $\theta_b, \phi_b$  and  $\psi_b$ . Fig. 28 shows the variation  $J$  with respect to  $\psi_b$  for the same case study. Also in this case the global minimum is correctly identified

**Table 4**

Range of orbital elements used in training set production.  $\Omega_{RAAN}$  was always set to zero such that the ascending node was at the same longitude as the telescope.  $\theta$  is bounded such that the object is overhead ( $\pm 15$  degrees) at the start of the simulation.

Orbital element	Value range
$a$ (km)	7471–7671
$e$	0–0.01
$i$ ( $^\circ$ )	–45–45
$\Omega$ ( $^\circ$ )	0
$\omega$ ( $^\circ$ )	0–359.9
$\theta$ ( $^\circ$ )	$(360 - \omega - 15) - (360 - \omega + 15)$

**Table 5**

Material distribution for the 3U cubesat simulation.

Cubesat Face (body axis)	Aluminium fraction	Solar Panel fraction
$+x$	0	1
$+y$	1	0
$+z$	1	0
$-x$	0	1
$-y$	1	0
$-z$	1	0

as 0 degrees. After applying the multi-start search, the optimisation algorithm was able to correctly identify the direction of the normal vector.

For the simple case analysed in this paper and a regular attitude motion, this approach has given good results that are easily explainable. For more complex geometries, material distributions and irregular attitude motions, the number of minima multiplies and a correct identification is not always easy. Future work is needed to account for the time variation of the spectra of the individual materials. This is expected to eliminate alternative minima and reduce the number of feasible solutions.

## 5.2. Attitude estimation with machine learning

We also propose an alternative approach for estimating the attitude which bypasses the unmixing of the spectra, and directly associates individual spectra to particular orientations of a given object.

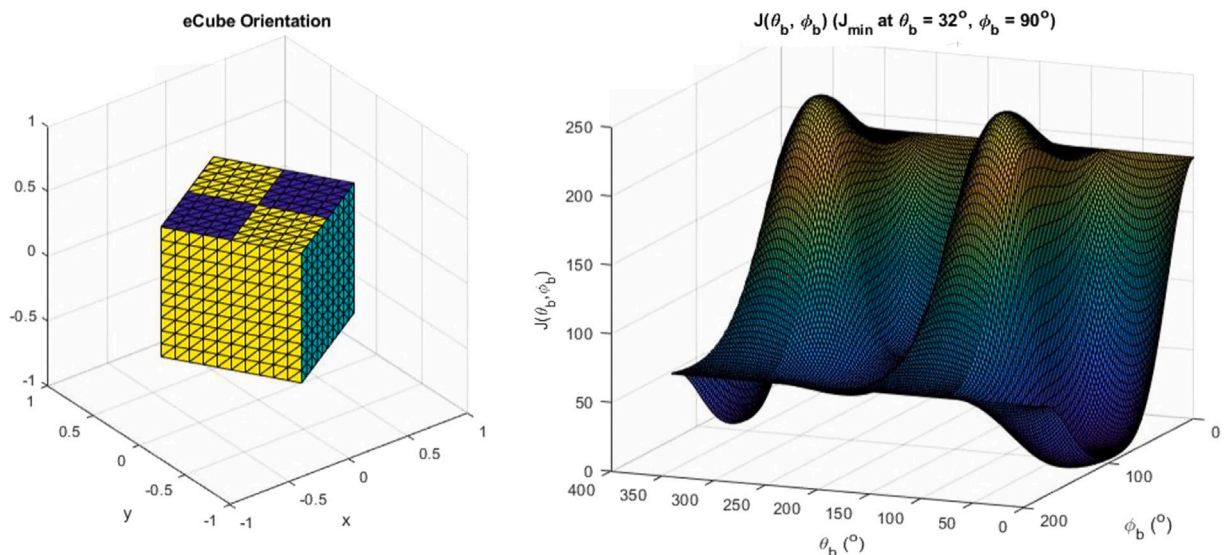


**Fig. 27.** Example of variation of  $J$  with respect to  $\theta_b, \phi_b$  for the true values of  $\theta_b = 32$  and  $\phi_b = 90$  and a phase angle of 45 degrees.

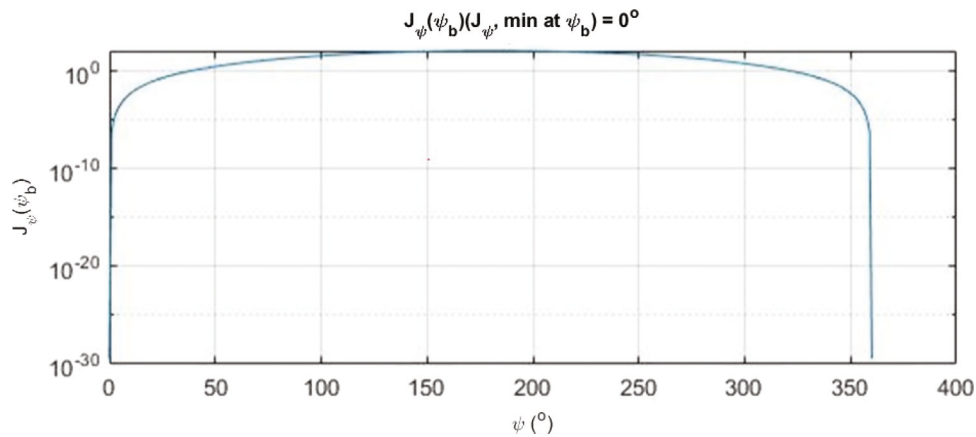


Fig. 28. Example of variation of  $J$  with respect to  $\psi_b$ .

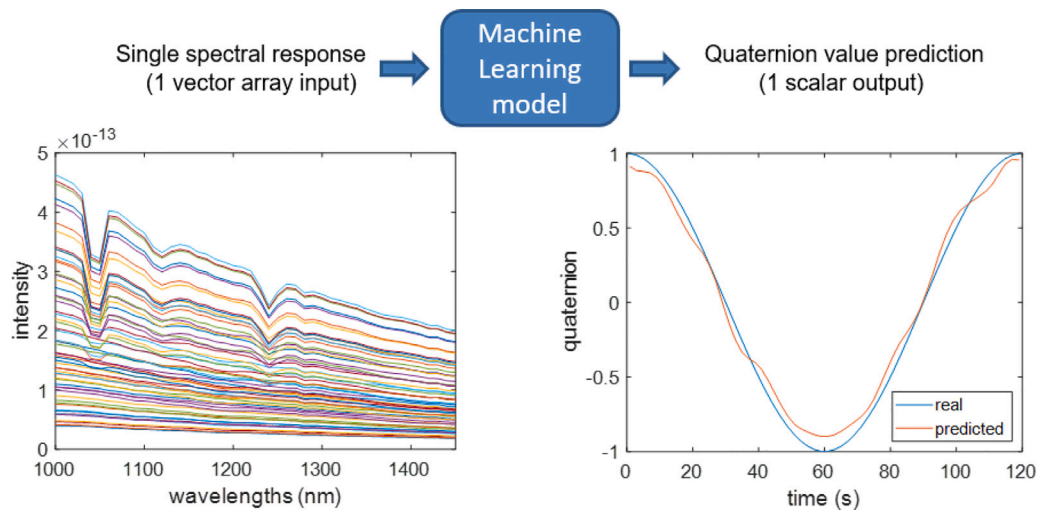


Fig. 29. Use of machine learning models for predicting quaternion values based on single spectral responses. In the initial experiment, the 60 spectra shown on the left side led to the predicted quaternion values on the right side with  $R^2 = 99.49$  and  $RMSE = 0.0755$ . Each time point corresponds to a 1-second integration from the sensor simulation.

### 5.2.1. 3U CubeSat

Initial simulations were performed for a more realistic scenario of a 3U cubesat in Earth orbit, with the telescope on ground. The cubesat was modelled as a  $30 \text{ cm} \times 10 \text{ cm} \times 10 \text{ cm}$  cuboid, with a simple distribution of materials as shown in Table 5, i.e. with two body-mounted solar panels covering two opposing long faces.

A series of simulations were performed to build a set of training data with which to train the machine learning models. To increase diversity of the training data, the orbital elements of the cubesat were initialised with uniform random variation within a range that allows a line of sight from the ground telescope. Table 4 shows the range used for each element. This range of orbital elements was chosen such that at the start of each observation arc, the object is within 15 degrees of the telescope zenith direction. The relatively high elevation angle was chosen due to the rapidly increasing atmospheric attenuation at lower elevation, likely rendering such small objects invisible before they cross the horizon. This approach results in range-bound random initial elevation rather than starting all simulations at some minimum elevation, as it is not known whether the orbits of objects will be known in advance of observations. Telescope location was held constant for each simulation at zero longitude and 5 degrees latitude. In these simulations, atmospheric attenuation is enabled, and the same wavelength bands as before are used.

In each simulation, the cubesat was set rotating about an axis offset from its long axis by 5 degrees to introduce a small nutation

motion. The magnitude of the angular velocity was randomly generated between 0 and 1 revolution per minute. The object's rotation was simulated for 5 min sampled at 1 Hz, yielding 300 quaternions and 300 corresponding spectra.

For this initial experiment, we developed a Support Vector Machine (SVM) regression model implemented using libsvm [30]. This was trained to extract the elements of the quaternions (one separate model for each quaternion element) representing the orientation at time  $t$ ,  $\mathbf{q}(t)$ , given only the corresponding received spectrum  $\mathbf{s}(t, \lambda)$ , where  $\mathbf{s}(t, \lambda_{ref})$  is the measured intensity at time  $t$  in an arbitrary reference band  $\lambda_{ref}$ . This transformation is a higher-resolution implementation of the colour indexing approach often used in astronomical observations [5].

Since predictions are made on a point-by-point basis, the data can be split 50–50 into training and testing sets by alternating assignment into each set, i.e. samples 1, 3, 5... comprised the training set and samples 2, 4, 6... comprised the test set. This ensures both sets contain samples from the full range of each parameter so that the model is not required to extrapolate [31–34].

Using this time-point-based prediction, Fig. 29 shows the results of an initial experiment in which a relatively small amount of data (a subset of one simulation instance, with 121 spectral responses, sampled at 1 s intervals, i.e., 0–120 s), with a promising prediction achieved with  $R^2 = 99.49$  and  $RMSE = 0.0755$ . This SVM model was implemented using a reduced dimensionality of the spectral responses (from 46 spectral bands to 5 main features) via Principal Component



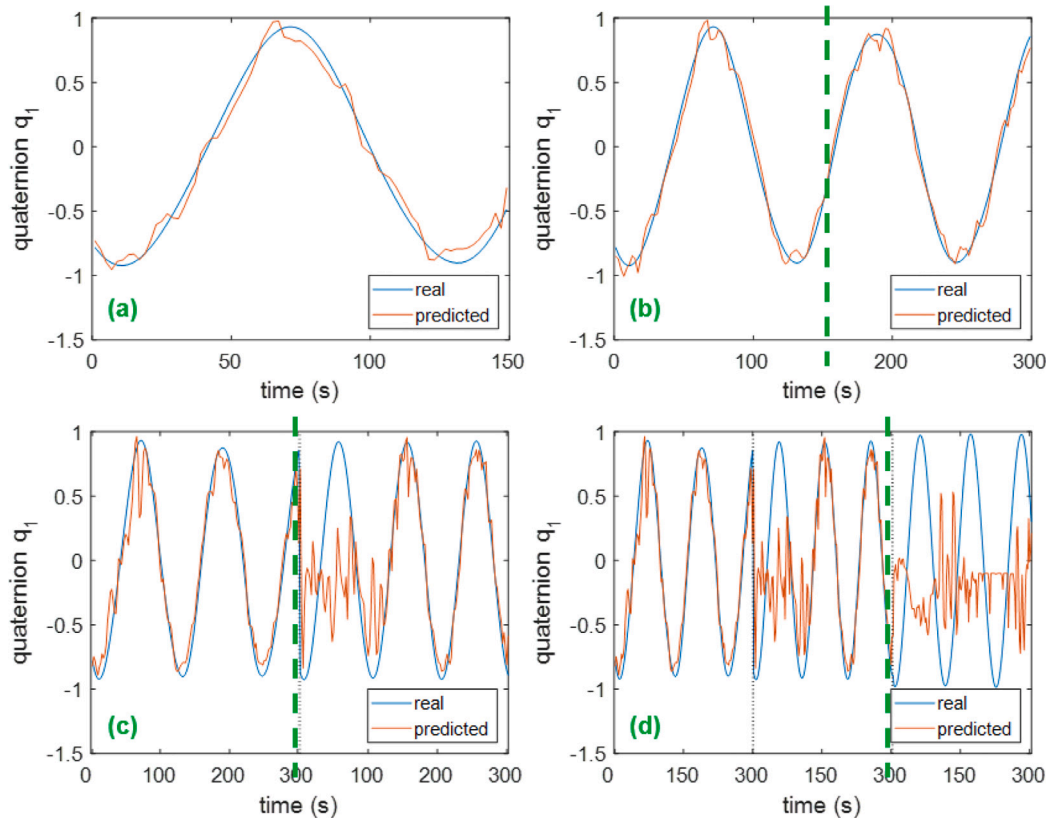


Fig. 30. Extended results of SVM regression (for quaternion  $q_1$ ) with progressive addition of new data. The right side of the green dashed line indicates where new data is introduced with relation to the previous experiment, showing that the addition of new data challenges the ability of the regression models to generalise: (a)  $R^2 = 98.72$ , (b)  $R^2 = 98.79$ , (c)  $R^2 = 74.73$ , and (d)  $R^2 = 34.09$ .

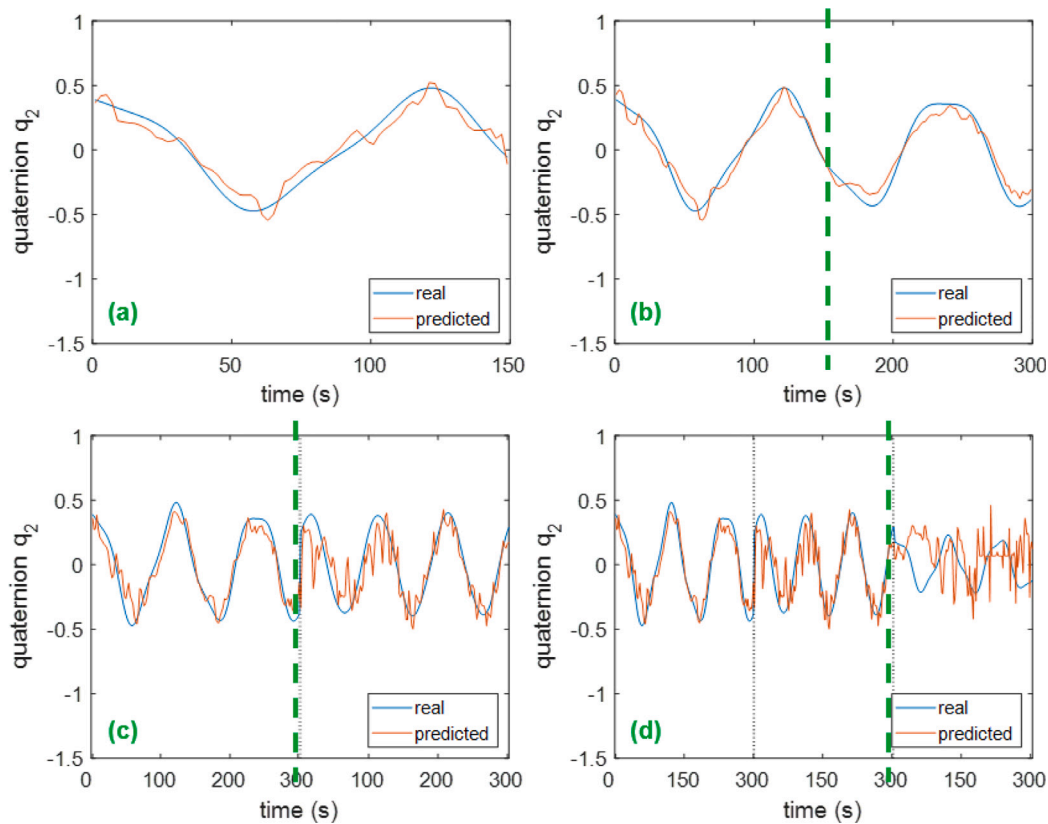


Fig. 31. Extended results of SVM regression (for quaternion  $q_2$ ) with progressive addition of new data. The right side of the green dashed line indicates where new data is introduced with relation to the previous experiment, showing that the addition of new data challenges the ability of the regression models to generalise: (a)  $R^2 = 94.06$ , (b)  $R^2 = 95.66$ , (c)  $R^2 = 82.51$ , and (d)  $R^2 = 56.79$ .

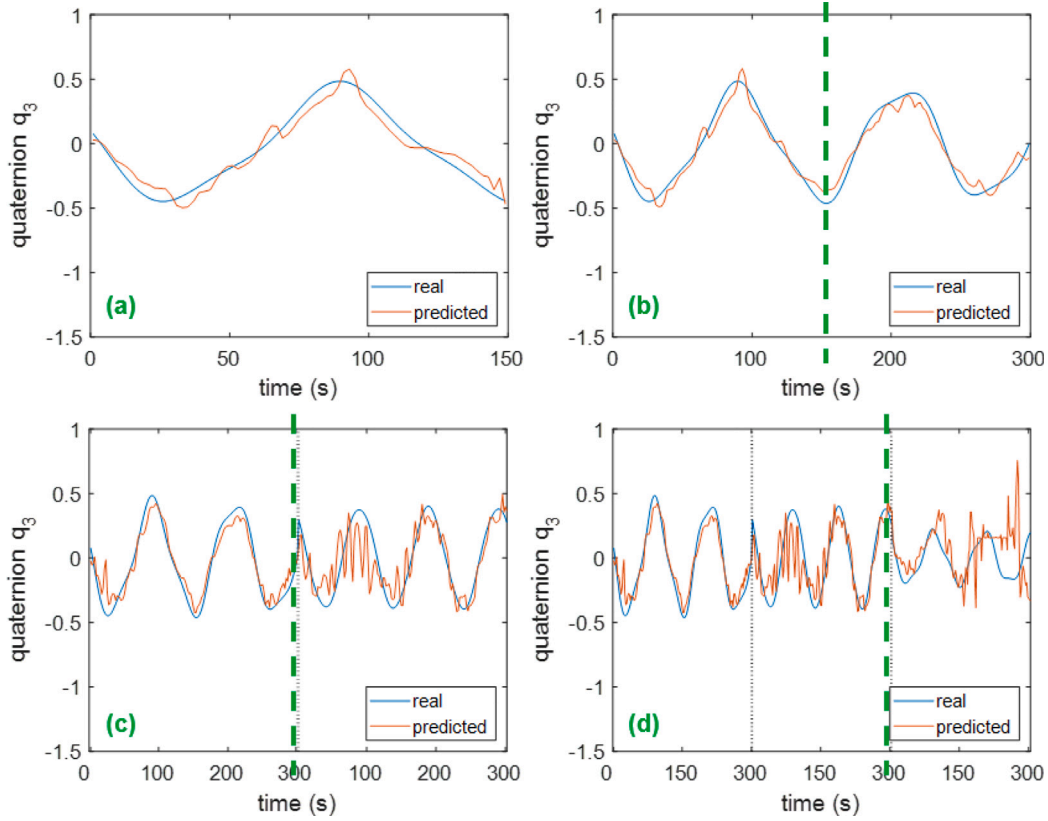


Fig. 32. Extended results of SVM regression (for quaternion  $q_3$ ) with progressive addition of new data. The right side of the green dashed line indicates where new data is introduced with relation to the previous experiment, showing that the addition of new data challenges the ability of the regression models to generalise: (a)  $R^2 = 93.34$ , (b)  $R^2 = 95.39$ , (c)  $R^2 = 80.52$ , and (d)  $R^2 = 58.61$ .

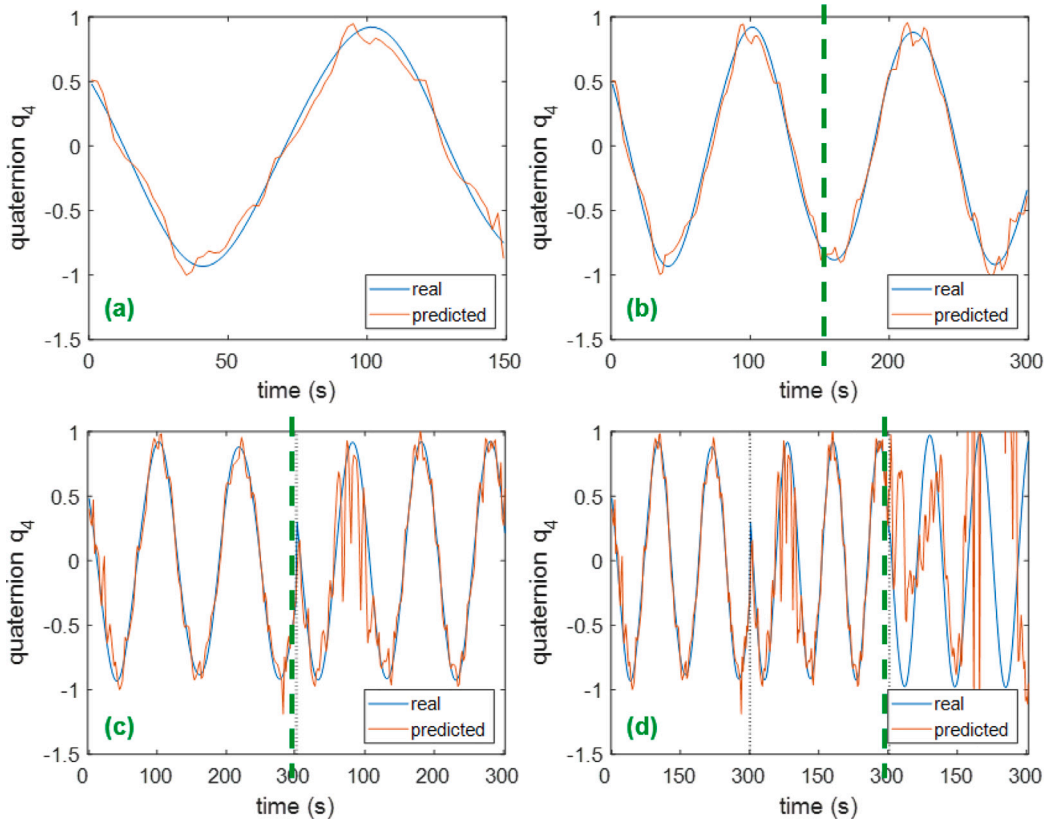


Fig. 33. Extended results of SVM regression (for quaternion  $q_4$ ) with progressive addition of new data. The right side of the green dashed line indicates where new data is introduced with relation to the previous experiment, showing that the addition of new data challenges the ability of the regression models to generalise: (a)  $R^2 = 98.31$ , (b)  $R^2 = 98.56$ , (c)  $R^2 = 92.56$ , and (d)  $R^2 = 31.84$ .

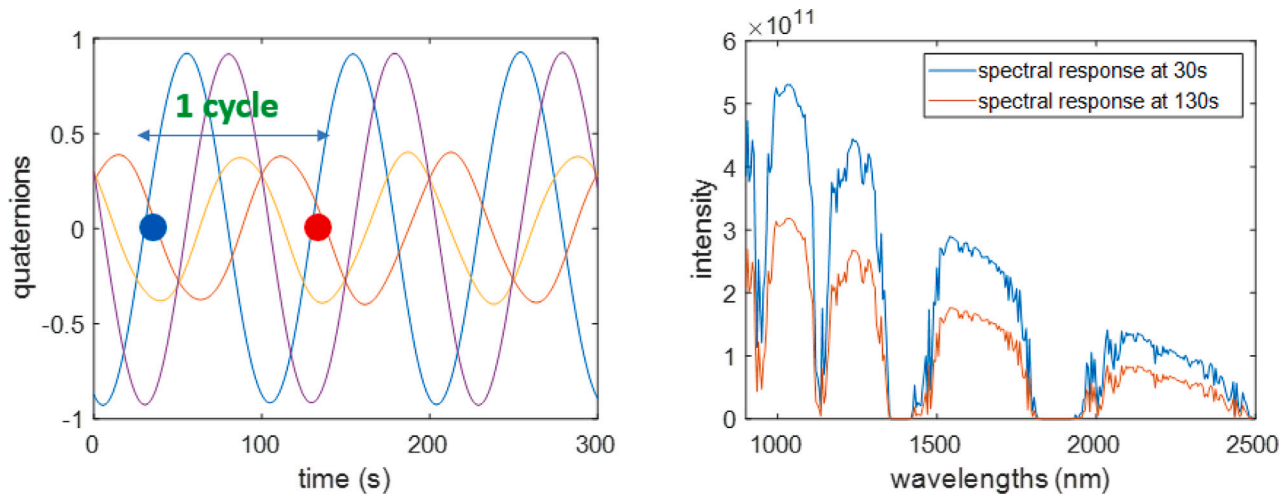


Fig. 34. Comparison of spectral responses corresponding to equivalent quaternions. While the value of the quaternions repeats cyclically, the spectral responses show an evolution over the time which challenges the ability of the regression models to generalise. (For interpretation of the references to colour in this figure legend, the reader is referred to the web version of this article.)

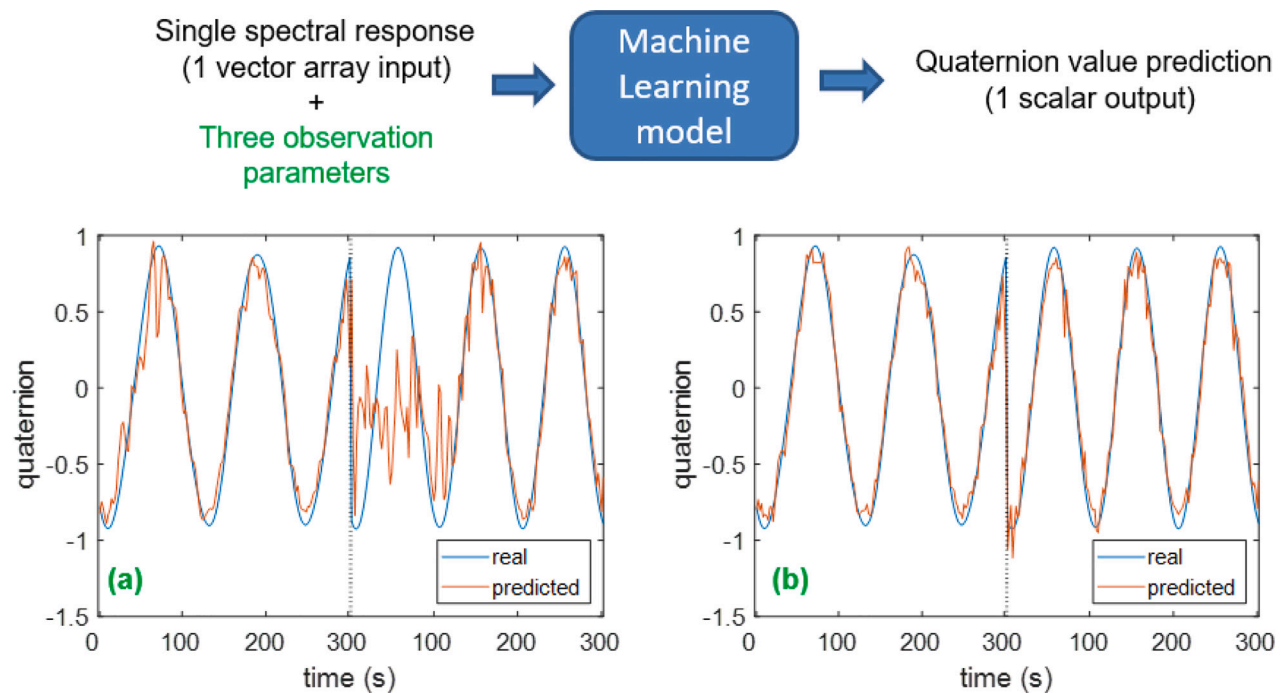


Fig. 35. Improved SVM prediction (for quaternion  $q_1$ ) with the inclusion of observation conditions and geometry: (a) result without observation conditions achieved  $R^2 = 74.73$  and RMSE = 0.3271, (b) result with observation conditions achieved  $R^2 = 97.97$  and RMSE = 0.0999. Similar improvement was found for the other quaternions.

Analysis (PCA) [35], which is a common feature extraction method used in combination with SVM regression.

After this initial experiment, we extended the SVM datasets to include multiple simulations (where we follow the same train–test split and only test on spectra from ‘seen’ simulations). We then attempted to make predictions on a totally unseen simulation instance which had not been used as a source of training samples using the alternating train–test split. Here we also increased the number of components from the PCA to 50. These results can be seen in Figs. 30–33 where the green dashed line indicates the addition of new data in the experiments. While the performance of the models was acceptable for a limited amount of data, the inclusion of larger data from different instances for training the models eventually led to worse performance. Taking quaternion  $q_1$  as example, Fig. 30(a) and (b) show a good performance with  $R^2 = 98.72$  and  $R^2 = 98.79$ , respectively, using the first half of

a simulation instance and the complete instance, with 301 time points (0–300 s). However, experiment in (c) shows how the addition of more data (a second simulation instance) can affect the performance ( $R^2 = 74.73$ ), as the model is not able to generalise well. Finally, experiment in (d) shows that the model fails to predict the quaternion ( $R^2 = 34.09$ ) for a third simulation instance which, in this particular experiment, was not considered in the training. A similar behaviour was found for the other quaternions.

The main reason why the SVM failed to generalise, was that the same quaternion, reoccurring at a later time, produced a different spectral response. This was due to the change in relative position of the object with respect to the observer, meaning for the same orientation, a different face may be visible. As well as this, the solar aspect angle changes as the object progresses along its orbit. This is illustrated

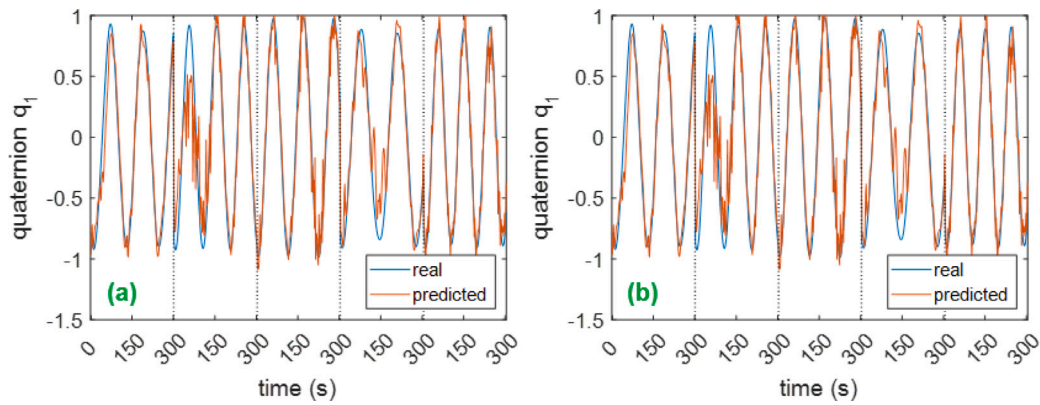


Fig. 36. Comparison between SVM and ANN prediction for quaternion  $q_1$  with the inclusion of observation conditions and geometry: (a) prediction results with SVM give an  $R^2 = 93.08$  and  $RMSE = 0.1752$ , (b) prediction results with ANN under the same conditions give an  $R^2 = 98.29$  and  $RMSE = 0.0861$ .

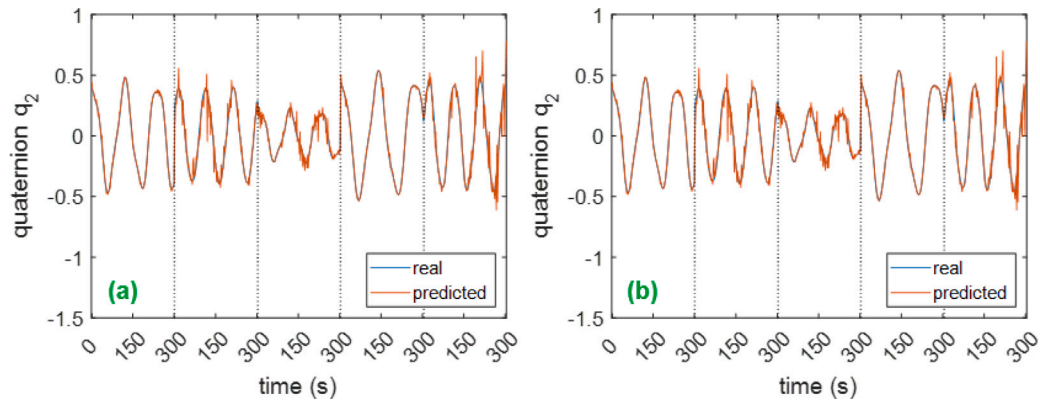


Fig. 37. Comparison between SVM and ANN prediction for quaternion  $q_2$  with the inclusion of observation conditions and geometry: (a) prediction results with SVM give an  $R^2 = 84.54$  and  $RMSE = 0.1125$ , (b) prediction results with ANN under the same conditions give an  $R^2 = 96.18$  and  $RMSE = 0.0563$ .

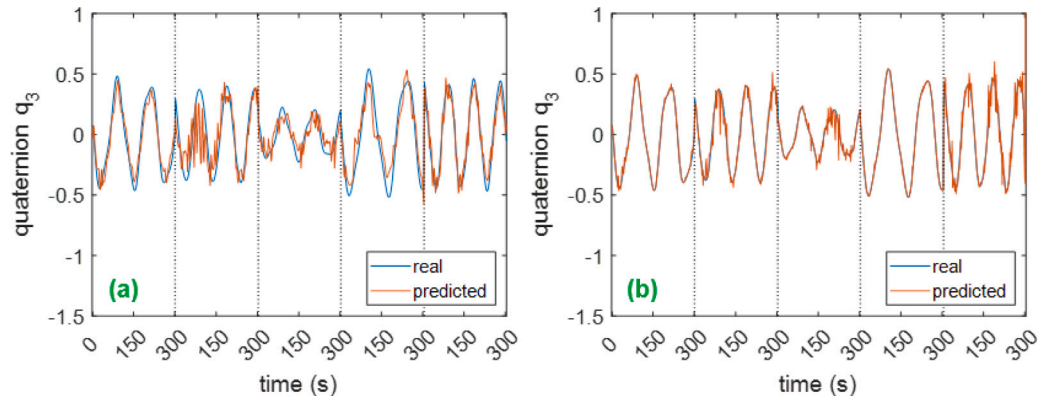


Fig. 38. Comparison between SVM and ANN prediction for quaternion  $q_3$  with the inclusion of observation conditions and geometry: (a) prediction results with SVM give an  $R^2 = 85.20$  and  $RMSE = 0.1104$ , (b) prediction results with ANN under the same conditions give an  $R^2 = 73.93$  and  $RMSE = 0.1642$ .

in Fig. 34, where an equivalent set of quaternions present different spectral responses (in blue and red colour, respectively).

To account for this, three additional features were included at each time point: the solar aspect angle, the distance to the object, and the unit vector pointing from the observer to the object.

Fig. 35 shows a comparison of the results obtained for the same train and test sets, with and without these additional observation parameters. This experiment included a total of 602 spectral responses (two independent simulation instances of 301 time points each, from 0–300 s). While the original prediction in Fig. 35(a) achieved  $R^2 = 74.73$  and  $RMSE = 0.3271$ , the inclusion of these parameters led to an improved  $R^2 = 97.97$  and  $RMSE = 0.0999$  in Fig. 35(b), showing

a significant improvement. Similar enhancement was achieved when predicting the other quaternions, demonstrating that prior knowledge can be used to refine the model prediction.

All previous machine learning experiments used SVM for regression tasks. However, machine learning regression could also be implemented via Artificial Neural Networks (ANN) [36], more powerful algorithms with, presumably, higher generalisation ability. In the next experiment see Figs. 36–39, more data (a total of 1505 spectral responses, five independent simulation instances of 301 time points each, from 0–300 s) is evaluated under the same conditions with the only difference that, in (a), the machine learning is based on SVM regression, while in (b), it is based on ANN regression. The NN consisted of



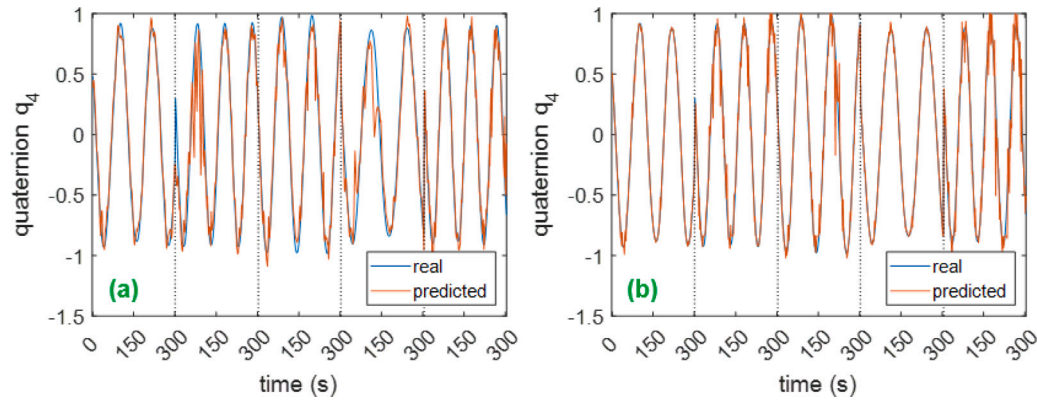


Fig. 39. Comparison between SVM and ANN prediction for quaternion  $q_4$  with the inclusion of observation conditions and geometry: (a) prediction results with SVM give an  $R^2 = 94.56$  and  $RMSE = 0.1505$ , (b) prediction results with ANN under the same conditions give an  $R^2 = 97.69$  and  $RMSE = 0.0971$ .

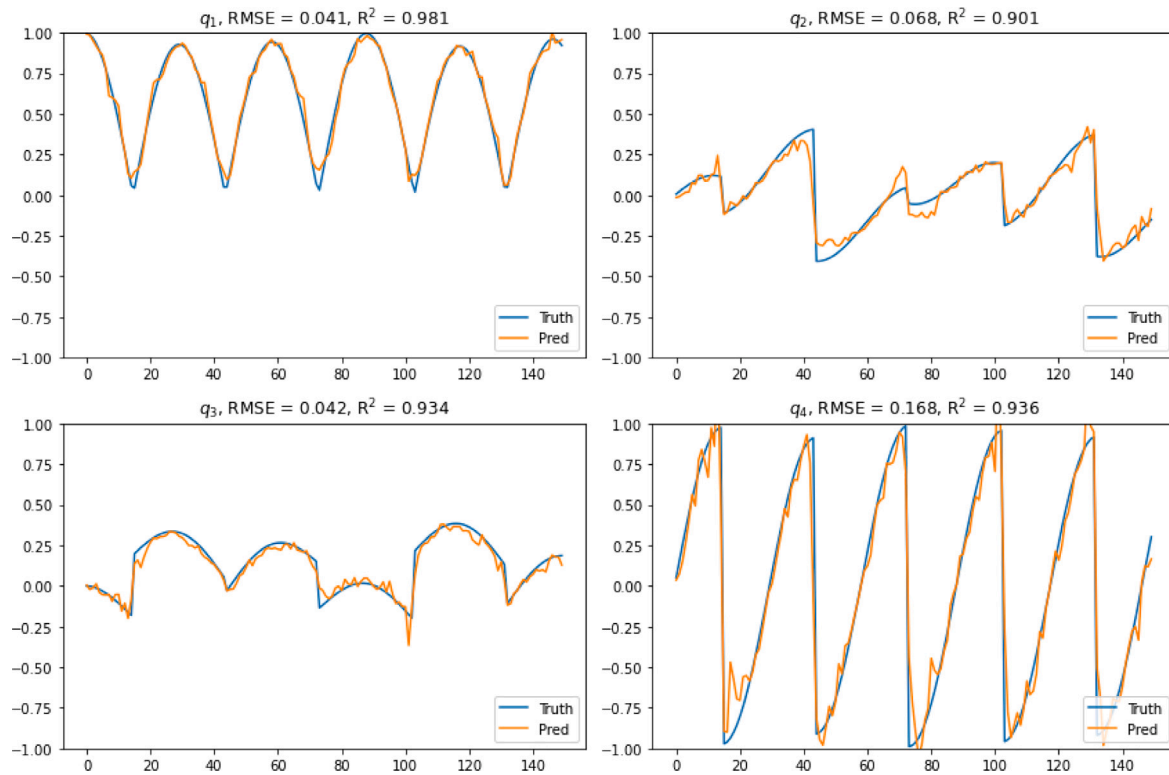


Fig. 40. True and predicted quaternions for the cube in orbit test case, using the ANN.

a relatively basic architecture, a feedforward fully-connected NN for regression (ReLU activation function), with input layer of the same dimensionality as the PCA components (50), a hidden layer with 100 nodes, plus a second hidden layer with 10 nodes, and an output layer of 1 node or value (the regression prediction). A separate NN was trained for each quaternion element. These were implemented and trained through the Matlab fitnet function (LBFGS solver). By replacing SVM regression with ANN regression, the prediction clearly improved in 3 of the 4 quaternions, going from  $R^2 = 93.08$  to  $98.29$  and  $RSME = 0.1752$  to  $0.0861$  for quaternion  $q_1$ . This improvement is in line with expectations and shows that NNs, yet more complex than SVMs, are able to provide more accurate predictions of the quaternions.

### 5.2.2. Asymmetric cube

A concern with the previous results is that the oversimplified, highly symmetrical nature of the 3U cubesat model causes an ever-present one-to-many mapping between spectra and orientations: for any orientation  $\mathbf{q}$  there are always 3 alternative orientations (rotations of 180

degrees) which appear the same to an observer and will result in the same spectrum. While the observation parameters help to disambiguate in a small dataset (since one of these alternative orientations must occur at a later time with different observation parameters), when the dataset becomes large enough (in an attempt to develop a more generalised model), the ambiguity will reappear and prevent good model convergence.

We then developed a more generalised model, using train/test data from simulations of a simple 30 cm cube with an asymmetrical material distribution, as described by Table 7. The cube's motion is simulated in Earth orbit, with orbital elements in Table 6. The diagonal elements of the inertia tensor were  $[0.6, 0.6, 1]$ , and the initial axis of rotation in the body frame was  $[0.1483, 0, 0.9889]$ , which induced a precessing rotation. The magnitude of the initial angular velocity was  $2\pi \text{ rad s}^{-1}$  and the body axes are aligned with the inertial axes at the start of the simulation.

Since the quaternions  $\mathbf{q}$  and  $-\mathbf{q}$  both correspond to the same orientation [37], in order to achieve robust convergence with machine

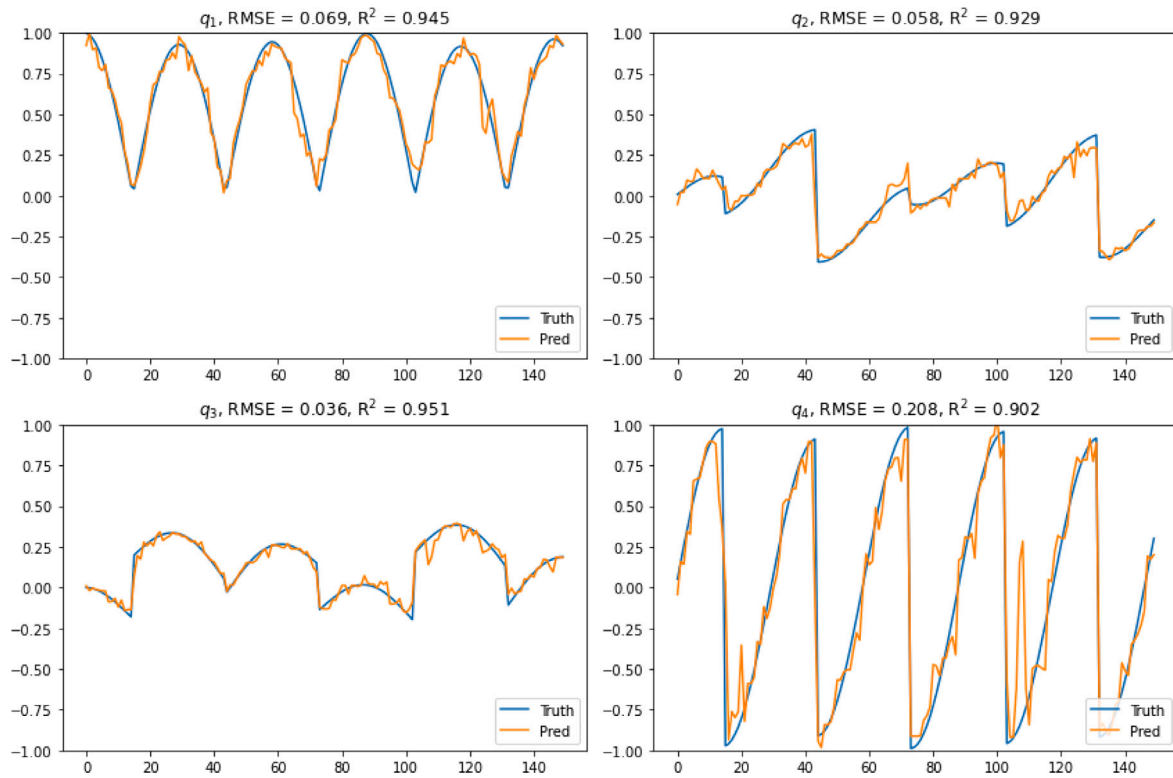


Fig. 41. True and predicted quaternions for the cube in orbit test case, using gradient boosted tree ensembles.

Table 6

Orbital elements for the cube in orbit.

$a$ (km)	$e$	$i(^{\circ})$	$\Omega(^{\circ})$	$\omega(^{\circ})$	$\theta(^{\circ})$
7596.3	0.0072	5.93	355.43	143.1	202.6

Table 7

Material distribution for ML-based attitude estimation.

Cube face (body axis)	Material
+x	Gold thermal blanket
+y	Aluminium
+z	GaAs solar panel
-x	Titanium
-y	White paint
-z	Red paint

Table 8

Hyperparameters for the ANN model.

Hyperparameter	Value
# Hidden layers	2
Dropout fraction	0.2
# Hidden nodes	200, 50
# Output nodes	4
Activation functions	ReLU - tanh - linear
Mini-batch size	16 samples
Optimiser	Adam

learning models employing gradient descent such as ANNs, one must restrict the solution space to remove this duplication of valid solutions. In this case we chose to restrict solutions to the half of  $\mathbf{q}$ -space where the first element of  $\mathbf{q}$ ,  $q_1$ , is non-negative, by making the transformation  $\mathbf{q}(t) \rightarrow -\mathbf{q}(t)$  when  $q_1(t) < 0$ .

A new sample scaling method was also introduced which removes the effect of distance on signal magnitude, while preserving band-to-band magnitude relationships within the same sample, was applied by making the transformation in Eq. (17).

$$s(t, \lambda) \rightarrow -2.5 \log_{10} \left( \frac{s(t, \lambda)}{s(t, \lambda_{ref})} \right) \quad (17)$$

Two regression models — an ANN [36], and a gradient boosted tree ensemble [38] were trained to predict the quaternion elements in a similar manner as before. The hyperparameters of the new ANN can be found in Table 8. The model was trained until 100 epochs of no improvement, at which point the weights and biases were reverted to the best found set during training.

The boosted tree models used a minimalist architecture to control overfitting, with a maximum tree depth of 2, and a maximum of 100

trees per ensemble. One ensemble was trained per element of the quaternion to be predicted. The final number of trees in each model after training were 100, 56, 97 and 60 for  $q_{1,2,3,4}$  respectively.

The results for both models can be seen in Figs. 40–41, in this case using the same alternating train–test split as before. It can be seen that the quality of the predictions is very good, with an  $R^2$  coefficient of  $> 0.9$  for all elements of the quaternions.

To test the models' ability to generalise, we generated multiple instances of the same cube, each following a different trajectory (different orbital elements), but with the same rotational dynamics. Initial orbital elements were randomly generated in the same ranges specified before in Table 4.

In this experiment we changed the train/test split such that the model is trained on all time points from 98 instances, and tested on all time points from a separate 2 instances which can be considered unseen. The results of the predictions for both models can be seen in Figs. 42–43. Although the performance is reduced compared with Figs. 40–41, it is clear that there is transfer between the different orbits and illumination conditions, and that likely with an increased dataset size spanning a wider range of orbits the model could generalise very well. However, the training set still consisted of the same set of rotational dynamics, and likely a new model would need to be trained for different rotational motions.

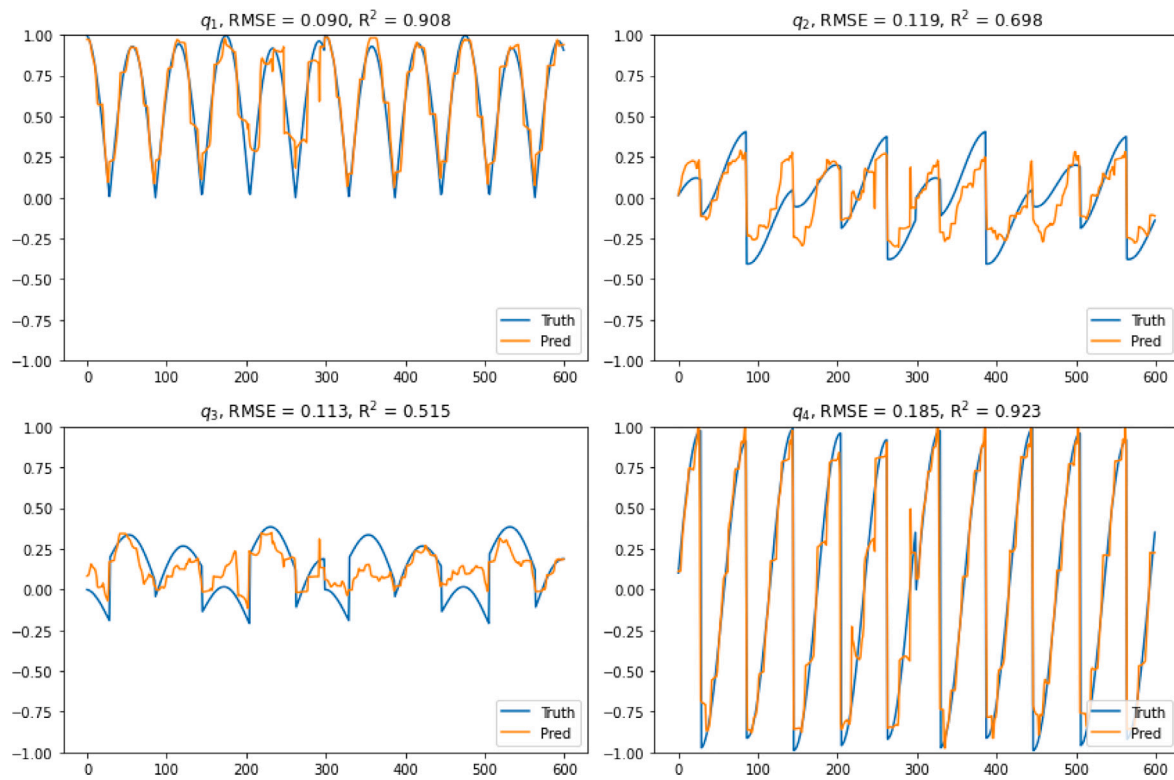


Fig. 42. ANN predictions of quaternions for the cube in orbit, testing on unseen instances.

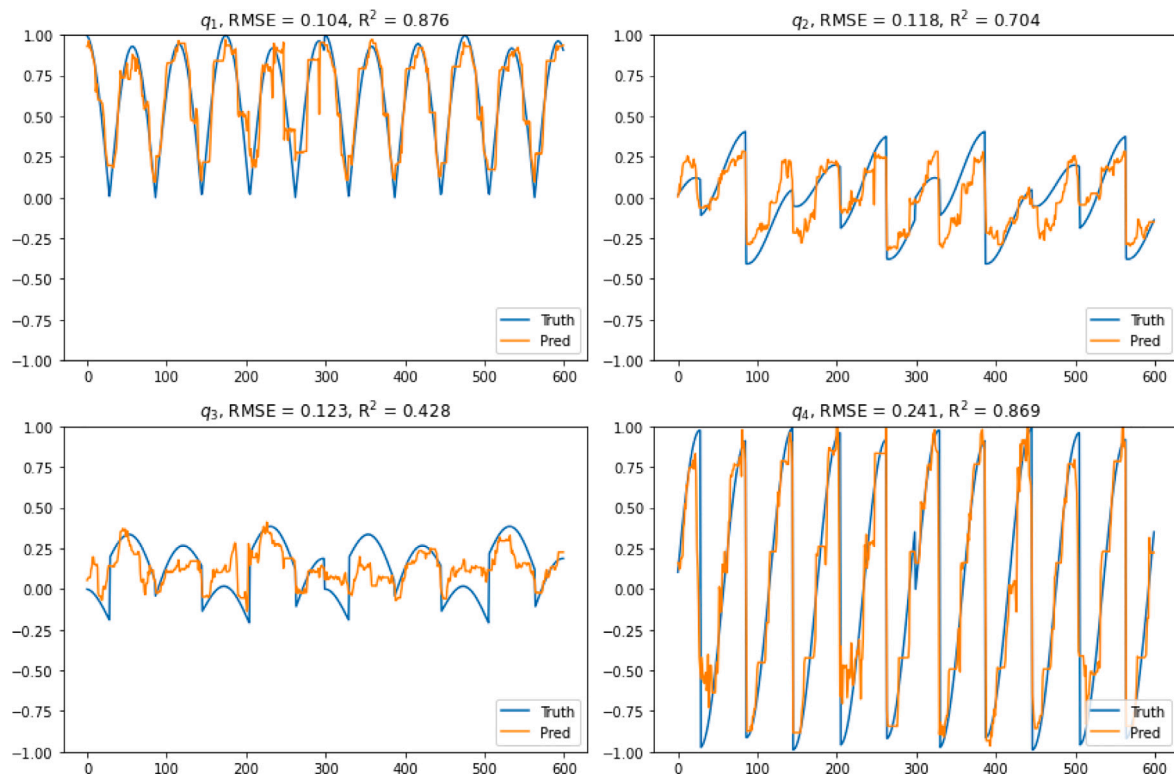


Fig. 43. Boosted tree ensemble predictions of quaternions for the cube in orbit, testing on unseen instances.

## 6. Final remarks

The paper presented some initial results on the use of hyperspectral imaging technology to characterise space objects. It was demonstrated,

through high fidelity simulations and laboratory tests, how one can extract the surface composition of unknown objects from single pixel observations. By looking at the spectrum received from a space object, one can unmix the signal and identify individual spectral components.

By comparing the individual spectra against a library of possible materials, one can infer the surface composition. Furthermore, it was demonstrated how an analysis of the time variation of the spectra can provide important indications on the attitude motion of the object in view, with a much richer information than traditional light curve methods. The paper proposed a simple measurement model that allows, under suitable assumptions on the expected shape of the object, the correct identification of the pointing direction of the outer faces of the object. Furthermore, we showed how the use of machine learning could offer a promising model-free solution to estimate the attitude motion by directly associating the spectra generated with our high fidelity model to corresponding quaternions at given times.

Although the simulation model presented in this paper accounts for a number of sources of attenuation and noise in the received spectra, the matching with a library of materials requires further steps to include weathering effects of the materials in space. Since the literature suggests much of the weathering effects manifest in the  $> 700$  nm spectral region, it is possible that shorter wavelengths contain sufficient information to match materials to observations. This would mean an accurate model may be constructed without the need to include these effects, however future work should verify this by attempting matching in the ultraviolet/visible regions. If this proves impossible, an accurate model of space weathering will likely be required to perform spectral matching as described in this paper. The next step is to produce a proper classification system that allows one to associate object classes to spectral signatures. This association will improve also the estimation of the attitude motion as different classes correspond to objects with reference shapes (cubesat, rocket bodies, telecom satellites, etc.) and expected components. A similar association of materials to surfaces can be derived from the endmember decomposition. This aspect will also be investigated in future work. Further work is also required to identify the most appropriate parameterisation to associate spectra to attitude motion and enable to learning the attitude kinematics from the time series of spectra.

### Declaration of competing interest

The authors declare that they have no known competing financial interests or personal relationships that could have appeared to influence the work reported in this paper.

### Acknowledgements

The work was partially supported by the UK Space Agency NSTP grant HyperSST.

### References

- [1] K. Jorgensen, J. Africano, K. Hamada, E. Stansbery, P. Sydney, P. Kervin, Physical properties of orbital debris from spectroscopic observations, *Adv. Space Res.* 34 (5) (2004) 1021–1025, <http://dx.doi.org/10.1016/j.asr.2003.02.031>, URL <https://www.sciencedirect.com/science/article/pii/S027311770400078X>.
- [2] K. Abercromby, M. Guyote, J. Okada, et al., Applying space weathering models to common spacecraft materials to predict spectral signatures, in: *Proceedings of AMOS Technical Conference*, Maui, Hawaii, USA, 2005.
- [3] J.A. Reyes, H.M. Cowardin, D.M. Cone, Characterization of spacecraft materials using reflectance spectroscopy, in: *Proceedings of the Advanced Maui Optical and Space Surveillance Technologies Conference*, Maui, Hawaii, September 11–14, 2018.
- [4] T. Cardona, P. Seitzer, A. Rossi, F. Piergentili, F. Santoni, BVRI photometric observations and light-curve analysis of GEO objects, *Adv. Space Res.* 58 (4) (2016) 514–527, <http://dx.doi.org/10.1016/j.asr.2016.05.025>, URL <https://www.sciencedirect.com/science/article/pii/S0273117716302113>.
- [5] X.-F. Zhao, H.-Y. Zhang, Y. Yu, Y.-D. Mao, Multicolor photometry of geosynchronous satellites and application on feature recognition, *Adv. Space Res.* 58 (11) (2016) 2269–2279, <http://dx.doi.org/10.1016/j.asr.2016.09.020>, URL <https://www.sciencedirect.com/science/article/pii/S0273117716305336>.
- [6] A. Vananti, T. Schildknecht, H. Krag, Reflectance spectroscopy characterization of space debris, *Adv. Space Res.* 59 (10) (2017) 2488–2500, <http://dx.doi.org/10.1016/j.asr.2017.02.033>, URL <https://www.sciencedirect.com/science/article/pii/S0273117717301461>.
- [7] A. Willison, D. Bédard, A novel approach to modeling spacecraft spectral reflectance, *Adv. Space Res.* 58 (7) (2016) 1318–1330, <http://dx.doi.org/10.1016/j.asr.2016.06.013>, URL <https://www.sciencedirect.com/science/article/pii/S0273117716303118>.
- [8] L. Lind, H. Laamanen, I. Pölönen, Hyperspectral imaging of asteroids using an FPI-based sensor, in: S.R. Babu, A. Hélière, T. Kimura (Eds.), *Sensors, Systems, and Next-Generation Satellites XXV*, 11858, International Society for Optics and Photonics, SPIE, 2021, pp. 65–78, <http://dx.doi.org/10.1117/12.2599514>.
- [9] W. C.J., M. Jah, Attitude estimation from light curves, *AIAA J. Guid. Control Dyn.* 32, No 5 (2009).
- [10] A. Dianetti, J. Crassidis, Light curve analysis using wavelets, in: *2018 AIAA Guidance, Navigation, and Control Conference*, 8–12 January Kissimmee, Florida, 2018.
- [11] Y. Matsushita, R. Arakawa, Y. Yoshimura, T. Hanada, Light curve analysis and attitude estimation of space objects focusing on glint, in: *1st International Orbital Debris Conference*, IOC, Sugar Land, Texas, USA, 2019.
- [12] P. Chote, J. Blake, D. Pollacco, Precision optical light curves of LEO and GEO objects, in: *The Advanced Maui Optical and Space Surveillance Technologies (AMOS) Conference*, 2019.
- [13] F. Santoni, E. Cordelli, F. Piergentili, Determination of disposed-upper-stage attitude motion by ground-based optical observations, *J. Spacecr. Rockets* 50 (3) (2013) 701–708, <http://dx.doi.org/10.2514/1.A32372>.
- [14] T. Yanagisawa, H. Kurosaki, Shape and motion estimate of LEO debris using light curves, *Adv. Space Res.* 50 (1) (2012) 136–145, <http://dx.doi.org/10.1016/j.asr.2012.03.021>, URL <https://www.sciencedirect.com/science/article/pii/S0273117712002113>.
- [15] E. Kerr, G. Falco, D.P. Nina Maric, P. Talon, E. Petersen, C. Dorn, S. Eves, N.S.O. Jaime Nomen, R.D. Gonzalez, Light curves for GEO object characterisation, in: *8th European Conference on Space Debris*, 2021.
- [16] K. McNally, D. Ramirez, A. Anton, D. Smith, J. Dick, Artificial intelligence for space resident objects characterisation with lightcurves, in: *8th European Conference on Space Debris*, 2021.
- [17] M. Esposito, Spectral imagers for relative navigation, on-orbit servicing and debris removal, in: *Clean Space Industrial Days*, ESA, 2018, URL [https://indico.esa.int/event/234/contributions/4070/attachments/3093/3801/2018CSID\\_MEspposito\\_SpectralImagersForRelativeNavigationOnOrbitServicingAndDebrisRemoval.pdf](https://indico.esa.int/event/234/contributions/4070/attachments/3093/3801/2018CSID_MEspposito_SpectralImagersForRelativeNavigationOnOrbitServicingAndDebrisRemoval.pdf).
- [18] N. Poojary, H. D'Souza, M.R. Puttaswamy, G.H. Kumar, Automatic target detection in hyperspectral image processing: A review of algorithms, in: *2015 12th International Conference on Fuzzy Systems and Knowledge Discovery, FSKD*, 2015, pp. 1991–1996, <http://dx.doi.org/10.1109/FSKD.2015.7382255>.
- [19] K. Jorgensen, J. Africano, K. Hamada, E. Stansbery, P. Sydney, P. Kervin, Physical properties of orbital debris from spectroscopic observations, *Adv. Space Res.* 34 (5) (2004) 1021–1025.
- [20] S. Katz, A. Tal, R. Basri, Direct visibility of point sets, in: *ACM Transactions on Graphics*, ACM, 2007, pp. 1–11.
- [21] A. Berk, P. Conforti, R. Kennett, T. Perkins, F. Hawes, J. Van Den Bosch, Modtran® 6: A major upgrade of the modtran® radiative transfer code, in: *2014 6th Workshop on Hyperspectral Image and Signal Processing: Evolution in Remote Sensing, WHISPERS*, IEEE, 2014, pp. 1–4.
- [22] D.W. Green, Magnitude corrections for atmospheric extinction, *Int. Comet Q.* 14 (1992) 55.
- [23] F. Kasten, A.T. Young, Revised optical air mass tables and approximation formula, *Appl. Opt.* 28 (22) (1989) 4735–4738.
- [24] W.A. Smith, E.R. Hancock, A unified model of specular and diffuse reflectance for rough, glossy surfaces, in: *2009 IEEE Conference on Computer Vision and Pattern Recognition*, IEEE Computer Society, 2009, pp. 643–650.
- [25] M.E. Winter, N-FINDR: an algorithm for fast autonomous spectral end-member determination in hyperspectral data, in: M.R. Descour, S.S. Shen (Eds.), *Imaging Spectrometry V*, 3753, International Society for Optics and Photonics, SPIE, 1999, pp. 266–275, <http://dx.doi.org/10.1117/12.366289>.
- [26] C.-I. Chang, Q. Du, Estimation of number of spectrally distinct signal sources in hyperspectral imagery, *IEEE Trans. Geosci. Remote Sens.* 42 (3) (2004) 608–619.
- [27] L. Drumetz, G. Tochon, J. Chanussot, C. Jutten, Estimating the number of endmembers to use in spectral unmixing of hyperspectral data with collaborative sparsity, in: P. Tichavský, M. Babaie-Zadeh, O.J. Michel, N. Thirion-Moreau (Eds.), *Latent Variable Analysis and Signal Separation*, Springer International Publishing, Cham, 2017, pp. 381–391.
- [28] N. Keshava, J. Mustard, Spectral unmixing, *IEEE Signal Process. Mag.* 19 (1) (2002) 44–57, <http://dx.doi.org/10.1109/79.974727>.
- [29] F.A. Kruse, A. Lefkoff, J. Boardman, K. Heidebrecht, A. Shapiro, P. Barloon, A. Goetz, The spectral image processing system (SIPS)—interactive visualization and analysis of imaging spectrometer data, *Remote Sens. Environ.* 44 (2–3) (1993) 145–163.
- [30] C.-C. Chang, C.-J. Lin, LIBSVM: a library for support vector machines, *ACM Trans. Intell. Syst. Technol.* 2 (3) (2011) 1–27.
- [31] P. Williams, K. Norris, Near-Infrared Technology in the Agricultural and Food Industries, American Association of Cereal Chemists, Inc., 1987.
- [32] J.S. Luypaert, M.H. Zhang, D.L. Massart, Feasibility study for the use of near infrared spectroscopy in the qualitative and quantitative analysis of green tea, *Camellia sinensis* (L.), *Anal. Chim. Acta* 478 (2003) 303–312.

- [33] T. Qiao, J. Ren, C. Craigie, J. Zabalza, C. Maltin, S. Marshall, Quantitative prediction of beef quality using visible and NIR spectroscopy with large data samples under industry conditions, *J. Appl. Spectrosc.* 82 (2015) 137–144.
- [34] M. Halstensén, U. Hundhausen, E.H. Esbensen, Partial least squares PLS1 vs. PLS2 – optimal input/output modeling in a compound industrial drying oven, in: Proceedings of the 61st SIMS Conference on Simulation and Modelling SIMS 2020, September 22–24, Virtual Conference, 2020, Finland.
- [35] I.T. Jolliffe, *Principal Component Analysis for Special Types of Data*, Springer, 2002.
- [36] K. Suzuki, *Artificial Neural Networks*, IntechOpen, Rijeka, 2013, <http://dx.doi.org/10.5772/3409>.
- [37] R. Parent, Chapter 2 - technical background, in: R. Parent (Ed.), *Computer Animation (Third Edition)*, third ed., Morgan Kaufmann, Boston, 2012, pp. 33–60, <http://dx.doi.org/10.1016/B978-0-12-415842-9.00002-2>, URL <https://www.sciencedirect.com/science/article/pii/B9780124158429000022>.
- [38] T. Chen, C. Guestrin, Xgboost: A scalable tree boosting system, in: Proceedings of the 22nd Acm Sigkdd International Conference on Knowledge Discovery and Data Mining, 2016, pp. 785–794.